Title

THE EVALUATION OF ERRORS EU TO COMPTON SCATTERING IN GAMMA-RAY EMISSION IMAGING

Author

Bruno, M.F.

Publication Date

1983-12-01

Lawrence Berkeley Laboratory
UNIVERSITY OF CALIFORNIA

THE EVALUATION OF ERRORS DUE TO COMPTON SCATTERING IN GAMMA-RAY EMISSION IMAGING

M.F. Bruno
(M.S. Thesis)

December 1983

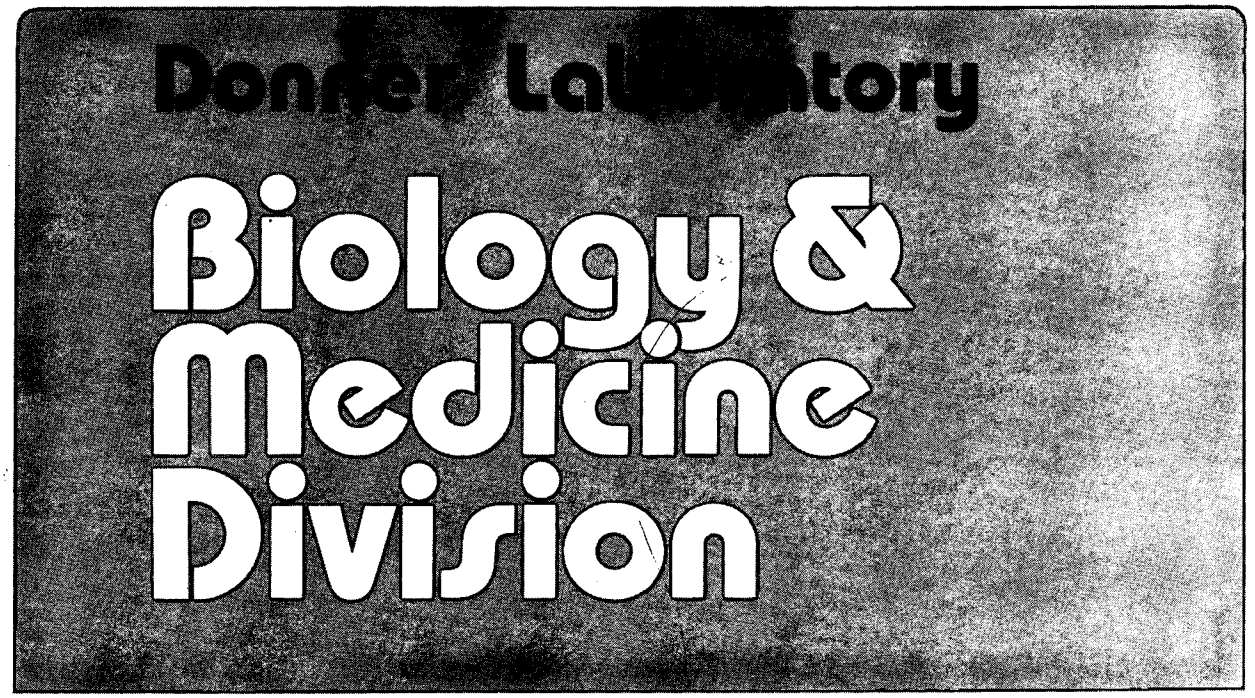

Prepared for the U.S. Department of Energy under Contract DE-AC03-76SF00098

DISCLAIMER

LBL-17385

THE EVALUATION OF ERRORS DUE TO COMPTON SCATTERING IN GAMMA-RAY EMISSION IMAGING

Michael Francis Bruno
M.S. Thesis

Lawrence Berkeley Laboratory
University of California
Berkeley, California 94720

December 1983

TABLE OF CONTENTS

ACKNOWLEDGMENTS

I would like to thank Dr. Thomas Budinger, Dr. Steven Derenzo and especially Dr. Ronald Huesman for extensive scientific assistance. I would also like to thank Dr. Kathleen Brennan for lending her technical expertise and Brian Knittel, who saved me several times in the last minute frenzy.

This work was supported by the Director, Office of Energy Research, Office of Health and Environmental Research of the U.S. Department of Energy under Contract No. DE-AC03-76SF00098 and by the PHS grant number HL25840 of the National Cancer Institute, DHHS.

December 19, 1983

MFB

SECTION 1 - THE SCATTER PROBLEM IN EMISSION COMPUTED TOMOGRAPHY.

1.1. Introduction.

One of the most important problems in emission imaging of radionuclide distributions is the background noise due to Compton scattered photons. Depending on the instrument design, between 10% and 50% of the detected events are actually unwanted scattered events. Three methods to control the amount of background from scattering are shielding or collimation, pulse height selection, and a posteriori image or projection data processing.

The events collected by a positron tomograph are true (unscattered) coincident events, scattered coincident events and accidental coincident events. Accidental coincidences in positron tomography are well understood, and several methods exist for accidental background subtraction. The scatter background in positron tomography is a more complicated problem and arises from both scatter in the object to be imaged and scatter in the tomograph. Scatter in the shielding is minimal, and scatter in the detectors can be rejected electronically, so that Compton scattering in the body is the remaining problem to be solved.

By making the shielding very deep, a single layer positron tomograph can be designed with sufficient shielding to virtually eliminate Compton scattered photons from the data acquisition process. However, the sensitivity to unscattered, image forming events would be very low. Therefore, there is a tradeoff which must be made between acceptance of scatter contaminated data and sensitivity of the tomograph[1].

For multilayer positron tomographs, the tradeoff between scatter and sensitivity is much more severe than that encountered with single layer systems. If cross-plane data (coincident events between different layers) are acquired, the in-plane shielding and scatter rejection must be less adequate than that for a corresponding single layer tomograph. For this reason, the Compton scatter background is a dominant physical problem in design considerations for multilayer positron tomographs.

The events collected by a single-gamma emission tomograph are true (unscattered events) and scattered events. Single-photon collimators cannot reject photons scattered in the body because scattered and unscattered photons cannot be differentiated geometrically; they differ only in energy. However, energy discrimination is more effective for the lower energy photons of commonly used single-gamma radionuclides than for 511 keV annihilation photons.

Several groups have realized the importance of the scatter background in emission computed tomography and have obtained varying degrees of success in attempting to make quantitative corrections for its effect. Scatter backgrounds have been measured or analytically characterized for sources in uniform attenuators[2-8], and some Monte Carlo simulations have been performed[9-11], but as yet the scatter background for a distributed source in a nonuniform distribution of attenuating media has not been characterized.

Scatter correction methods are important for quantitative positron tomographic studies because concentration measurements made from moment-to-moment or from region-to-region in a tomograph can be in error by as much as 50% unless appropriate compensation is made. There is no general

method for scatter compensation which is applicable to the class of circular detector arrays employed in positron tomographs, nor is there an acceptable method for scatter correction in single photon tomography which is being developed at many institutions around the world for widespread clinical application.

The work presented here represents the first step towards a general algorithm for scatter correction. Although the Monte Carlo simulation methods employed require too great a computational effort for routine use, they are extremely useful because they allow one physical effect to be modeled in the absence of any masking effects. They also allow simplifying assumptions to be tested. One might, for example, be able in many situations to ignore all but single scatters. Then, if the effect of single-scattered photons from a point source could be represented as an attenuator-dependent integral convolution in projection, a simple iterative scatter correction method could be devised.

1.2. Basic Physics.

There exist several physical processes which prevent the errorless measurement of radiation source positions in medical imaging. These processes fall mainly into two categories: nuclear effects which make localization impossible before the gamma radiation has been produced, and other effects which stem from the interaction of detectable gamma radiation with matter which intervenes between the source and the detector. Positron range and angulation are examples of processes in the first category. This type of effect, though important, will not be discussed here. Our concern lies instead with effects of the second type -- mainly photoelectric absorption and Compton scattering. These effects

predominate for gamma ray energies of interest in diagnostic medical imaging in materials with characteristics like those in living tissue. This is illustrated in Figure 1.1. Note that for energies less than 1 MeV, positron-electron pair production is negligible for essentially all materials.

In the photoelectric interaction of a gamma ray with an atom, the gamma ray is completely absorbed. Momentum is conserved through the recoil of the entire atom, while the photon energy is transferred to a single (formerly) bound electron. This energy appears only partially as kinetic energy in the electron, since some energy is required to overcome the electron-nucleus binding potential. The distribution of energy is described by the classic relation

$$T = h\nu - B_e \tag{1.1}$$

where $h\nu$ is the energy of the incoming gamma ray, T is the resulting kinetic energy of the electron, and B_e is the electron binding energy. The electron, which is ejected from the atom, usually resides in the atomic K-shell. The process is shown schematically in Figure 1.2.

Since the binding energy of an electron in an atomic K shell is usually less than 100 KeV, it is reasonable to inquire about the fate of the swift electron produced in a photoelectric collision. In particular, will an electron with kinetic energy T=400 KeV produce, in some interaction with its surroundings, secondary radiation which might still be detectable? This question can be answered by an examination of the scattering cross sections associated with the most common interactions of electrons with other electrons and with atomic nuclei. Of these

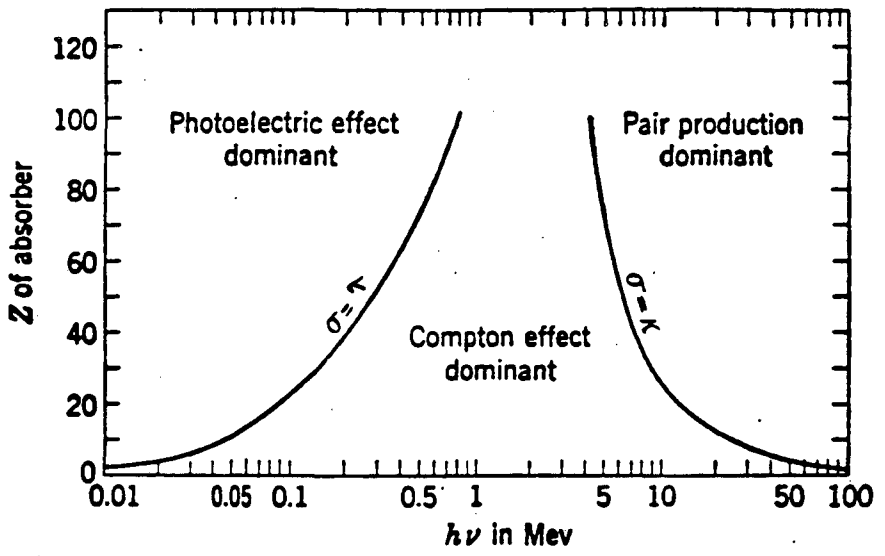

Figure 1.1

Regions of predominance for photoelectric effect, Compton scattering and pair production. For points on the two lines, neighboring effects have equal importance. Reproduced from Evans[12].

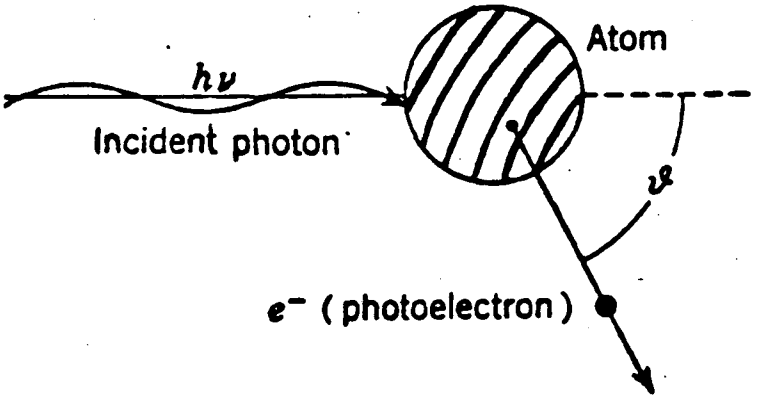

Figure 1.2

Schematic representation of the photoelectric effect. Reproduced from Evans[12].

interactions, it is only in the deflection of an electron by the Coulomb field of the nucleus that high-energy radiation is produced. In such an interaction, the electron may lose any fraction of its kinetic energy including the fraction f=1.

Table 1.1 gives the cross sections in barns/atom(1 barn = $10^{-24}cm^2$)in lead and air for ionization, nuclear elastic back scattering, electron-electron inelastic scattering, and Bremsstrahlung-producing deflections[12]. It also gives the approximate variation of each cross section with the atomic number Z and the quantity $\beta = v/c$, where v is the velocity of the incoming electron and c is the speed of light. In the table, the electron energy was taken to be 100 KeV. Since the value of Z for tissue can be roughly assumed to be similar to that of Carbon (Z=12), the data in Table 1.1 show that we can safely ignore any Bremsstrahlung radiation caused by photo-electrons.

	Ionization	Nuclear elastic backward scattering $\vartheta \geq 90°$	Electronic (inelastic) scattering $\vartheta \geq 45°$	Bremsstrahlung	
				σ_{rad}	σ'_{rad}
Approximate variation with Z and β	Z/β^4	Z^2/β^4	Z/β^4	Z^2	Z^2/β^2
Air	1,700	150	230	0.16	1.3
Pb	13,700	20,000	2,600	21	170

Table 1.1

Approximate cross sections in barns/atom for common electron interactions. Values shown are for 100 KeV electrons. Reproduced from Evans[12]

In Compton scattering, in contrast to the photoelectric effect, the gamma photon is not completely absorbed and it is assumed to interact with an unbound electron. This assumption is valid in cases when the energy of the gamma ray is very large compared to the binding energy of the electron. This requirement is satisfied in tissue scattering. In the collision of a photon with a free electron, momentum as well as energy is conserved between the two particles. Consideration of this circumstance leads to the fundamental Compton equation relating the energies of the incoming and outgoing photon to the scatter-angle denoted here by χ:

$$\frac{\nu'}{\nu_0} = \frac{1}{1 + \alpha(1-\cos\chi)} \quad , \tag{1.2}$$

where ν_0 is the incoming energy, ν' is the outgoing energy, $\alpha = h\nu_0/m_0c^2$, m_0 is the electron rest mass, and c is the speed of light in vacuum. To conserve momentum, the trajectories of the incident photon, outgoing photon and struck electron must be coplanar. The scattering angle χ is defined in this plane as shown in Figure 1.3. The remaining ambiguity in the direction of the scattered photon can be resolved by specifying the azimuthal angle ω, defined as in Figure 1.4.

The energy of the recoil electron is simply related to that of the two photons via

$$T = h\nu_0 - h\nu' \quad . \tag{1.3}$$

In this case, as with photo-electrons, secondary radiation produced by the electron is negligible.

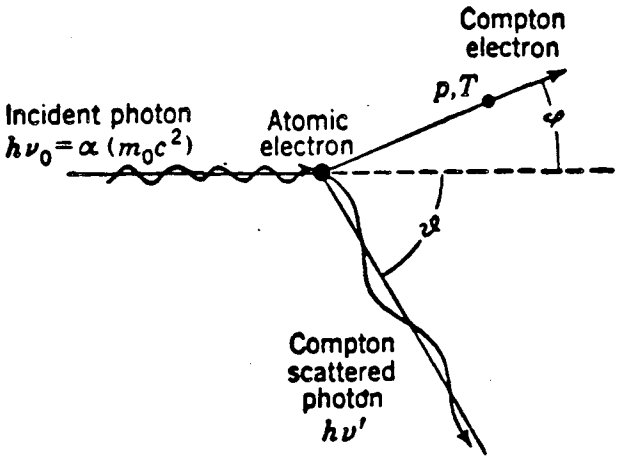

Figure 1.3

Schematic representation of a Compton Interaction. Reproduced from Evans[12].

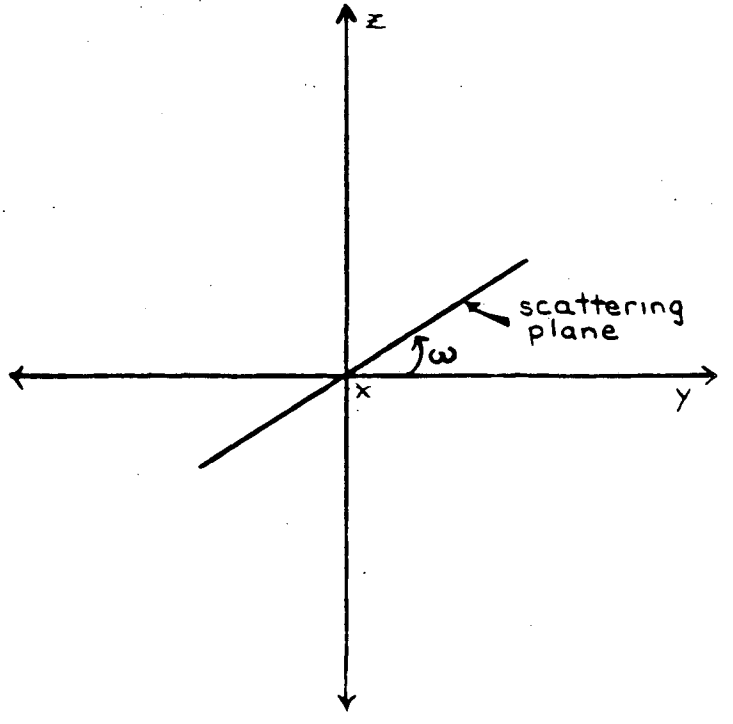

Figure 1.4

Definition of the azimuthal scattering angle, ω. The direction of the incident photon is along the x-axis (out of the page).

The differential Compton collision cross-sections of Klein and Nishina provide an extremely important description of the relative likelihood of scatter into an element of solid angle as a function of incoming energy:

$$\frac{d\sigma}{d\Omega} = \frac{r_o^2}{2} \left(\frac{\nu'}{\nu_o}\right)^2 \left(\frac{\nu_o}{\nu'} + \frac{\nu'}{\nu_o} + \sin^2\chi\right) \quad . \tag{1.4}$$

The value of $d\sigma/d\Omega$ derived from this formula is plotted in Figure 1.5 for various values of α. Note that forward scattering increases very strongly with increasing α. Of particular interest in positron emission imaging is the curve corresponding to $\alpha = 1$, the positron rest-mass energy.

It is important to recall that (1.4) represents the probability of scatter into a unit of solid angle at the scattering angle χ. The dependence of the probability on the variation of solid angle with χ can be removed using the relation

$$d\Omega = 2\pi \sin\chi \, d\chi \quad . \tag{1.5}$$

This yields a formula for the probability of any scatter which results in an outgoing photon direction along χ. This function is graphed in Figure 1.6. This plot emphasizes the fact that $d\Omega$ goes to zero as χ goes to zero, so that forward scatters into very small angles do not dominate the angular distribution as one might conclude from Figure 1.5.

The fundamental Compton equation can be simply solved for $\cos\chi$, suggesting the following decomposition of (1.4) for a cross section in the outgoing energy

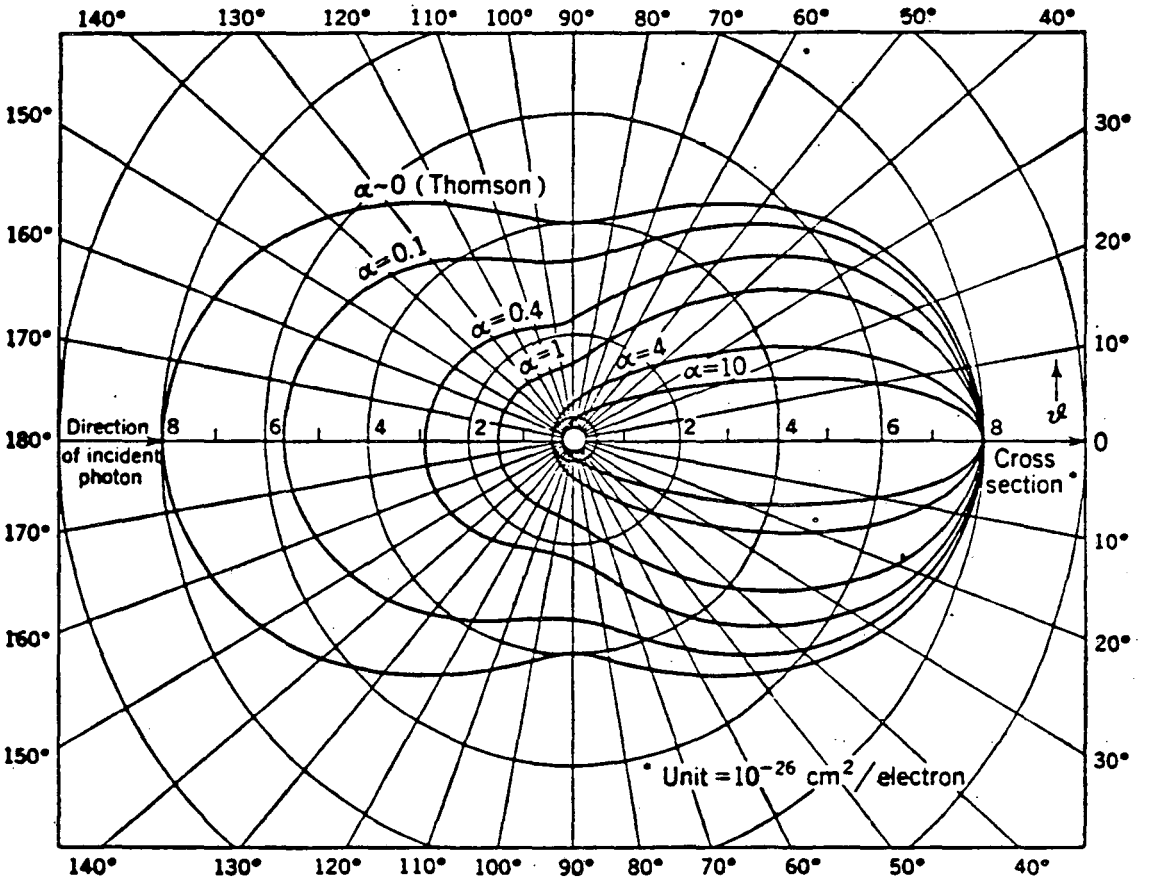

Figure 1.5

Polar plot of the relative number of photons scattered into a unit of solid angle in the direction of the scattering angle χ. Reproduced from Evans[12].

Klein-Nishina Cross Section in Scattering Angle χ

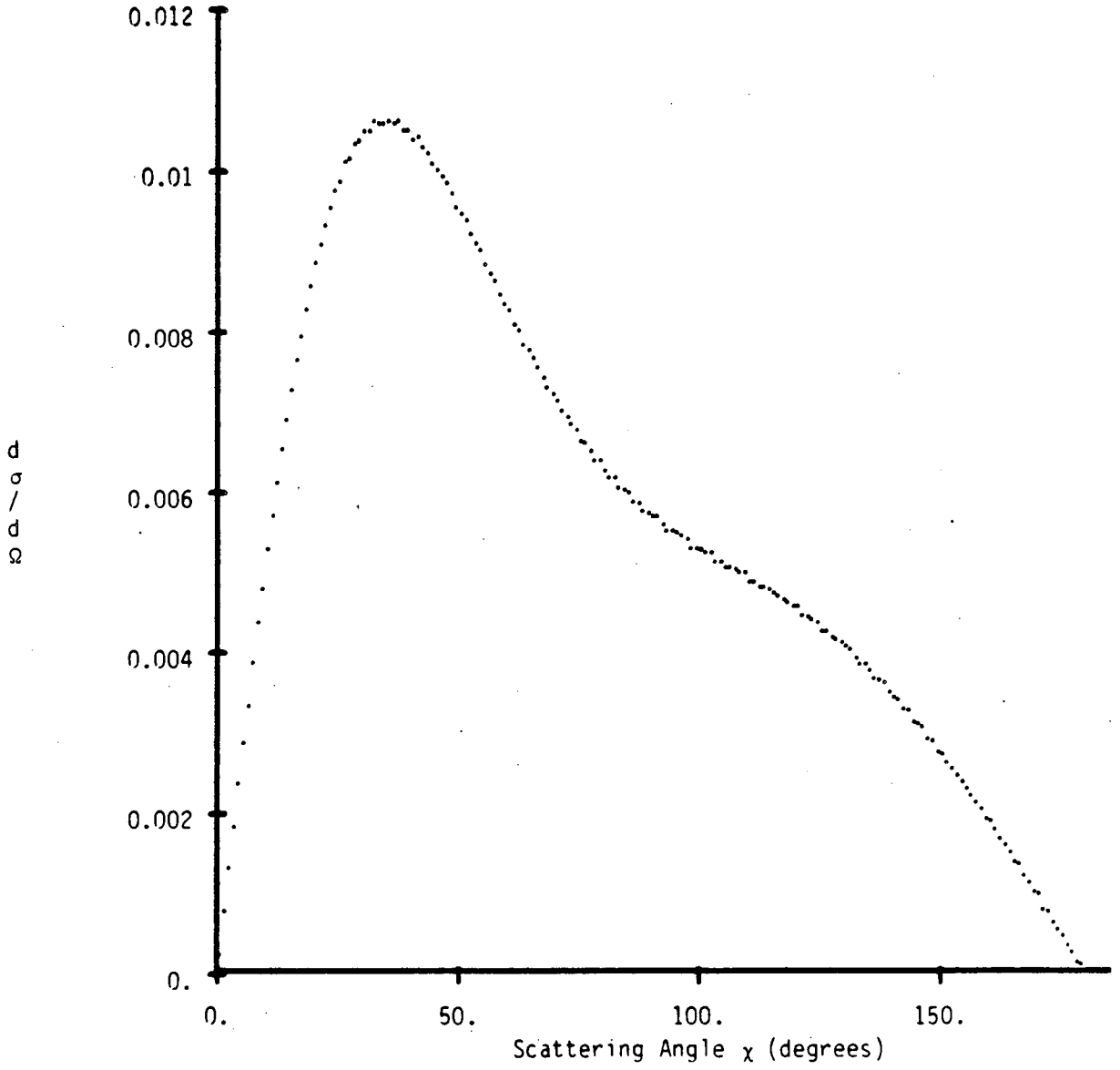

Figure 1.6

Probability of occurrence for a Compton scatter into the scatter angle χ.

$$\frac{d\sigma}{dh\nu'} = \left(\frac{d\sigma}{d\Omega}\right)\left(\frac{d\Omega}{d(\cos\chi)}\right)\left(\frac{d(\cos\chi)}{dh\nu'}\right) \tag{1.6}$$

Noting that (1.5) can be rewritten as $d\Omega = -2\pi\, d(\cos\chi)$ and differentiating (1.2) after solving for $\cos\chi$ we obtain

$$\frac{d\sigma}{dh\nu'} = \frac{\pi r_o^2 mc^2}{(h\nu)^2}\left\{\frac{h\nu'}{h\nu} + \frac{h\nu}{h\nu'} - 2\left(\frac{mc^2}{h\nu'} - \frac{mc^2}{h\nu}\right) + \left(\frac{mc^2}{h\nu'} - \frac{mc^2}{h\nu}\right)^2\right\} . \tag{1.7}$$

1.3. The Effect of Scatter in Emission Imaging.

Compton scattering and photoelectric absorption cause radiation detection systems to make errors in their estimation of both source position and source strength. The occurrence of source position errors is illustrated in Figure 1.7. In single photon imaging, the source is placed by the detection system at the position of the last scatter. In positron emission imaging, the scattered event is placed on a chord drawn between the positions at which the two scattered photons strike the detector.

The way in which photoelectric absorption affects source strength measurements is obvious. Compton scattering causes source strength estimation errors because the energy of any photon which emerges from a Compton scatter is lower than that of the incoming photon. Compton-scattered photons are therefore more susceptible to photoelectric absorption and have energies for which the detector may be more or less sensitive than it is at the unscattered energy.

Without resorting to Monte Carlo methods, it is difficult to make

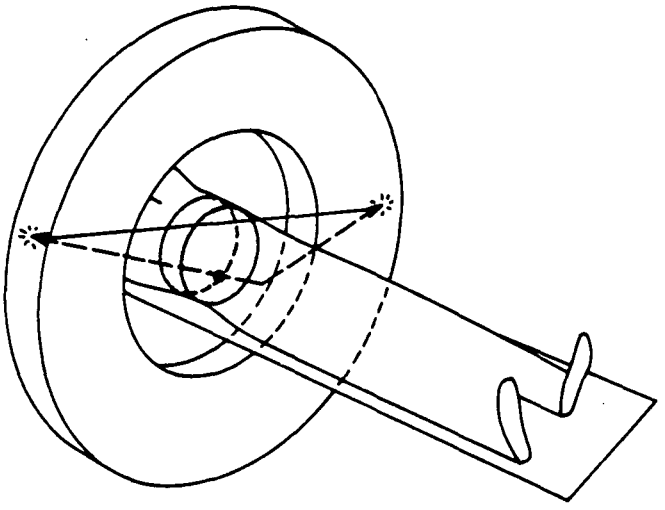

Figure 1.7

Illustration of the occurence of source localization error due to Compton scattering in positron emission tomogaphy (PET). The system erroneously places the event on the solid line.

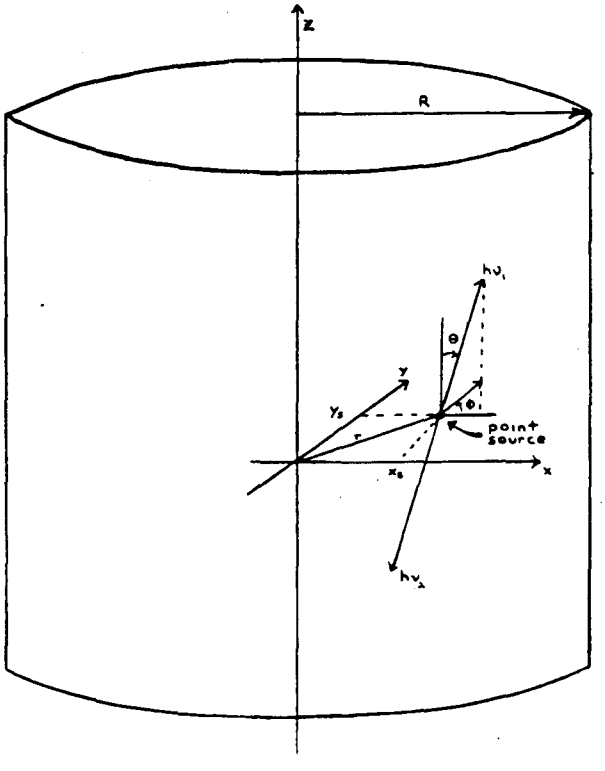

Figure 1.8

Source and attenuator geometry for equations (1.9) - (1.11) and Figure 1.9.

any quantitative statements about the spatial characteristics of the scatter background in the case of multiple scatters. However, some progress can be made in an analytical examination of the reduction in apparent source strength under these conditions. Using the Compton attenuation coefficient, one can estimate the magnitude of the scatter problem by calculating the fraction of emitted photons which escape a particular attenuator without scattering. Since these unscattered events will comprise the vast majority of counts registered in bins corresponding to actual source positions, the unscattered fraction is a good estimate of the reduction in source strength which will be reported by systems which do not correct for this attenuation.

Consider the geometry in Figure 1.8, which consists of a point source in a uniform attenuating cylinder of infinite length. The source lies in the x-y plane at a distance r from the axis of the cylinder (i.e., it has coordinates (x_s,y_s) with $x_s^2 + y_s^2 = r^2$), the radius of the cylinder is R and the Compton attenuation coefficient is μ. The probability that a photon emitted with direction angles θ and ϕ will escape the attenuator without scattering is simply

$$p = e^{-\mu \Delta r_b(\theta,\phi)} \quad , \tag{1.8}$$

where Δr_b is the distance from the source to the boundary of the attenuator along the direction of flight. The fraction of unscattered photons, f, is obtained by integrating this expression over all directions of emission with proper normalization

$$f = \frac{1}{4\pi} \int_0^{\pi} d\theta \int_0^{2\pi} d\phi \, \sin\theta \, e^{-\mu \Delta r_b(\theta,\phi)} \tag{1.9}$$

In single-photon imaging[13],

$$\Delta r_b = \frac{\sqrt{R^2 - r^2 \sin^2\phi} - r \cos\phi}{\sin\theta}, \tag{1.10}$$

while in positron-emission imaging[13]

$$\Delta r_b = \frac{2\sqrt{R^2 - r^2 \sin^2\phi}}{\sin\theta} \, . \tag{1.11}$$

The integral in (1.7) was evaluated numerically and the results are shown in Figure 1.9. The likelihood of unscattered escape does not increase appreciably with distance from the axis for positron-pair gamma rays because when one photon has a very short escape path, the path for the other becomes very long. This effect is accentuated by the three dimensional geometry of the calculation including the infinite length of the attenuator.

The analysis above, of course, is incomplete in one respect: it tells us nothing about the fate of the photons which do scatter. Without perfect energy resolution, a radiation detector will accept many of these events. One might argue that the fractions calculated above are not a good estimate of the quantitation errors due to scattering since a correction for this attenuation is relatively straightforward. The real problem is caused by the scattered events which are registered in bins which actually contain no source. The error represented by these mis-

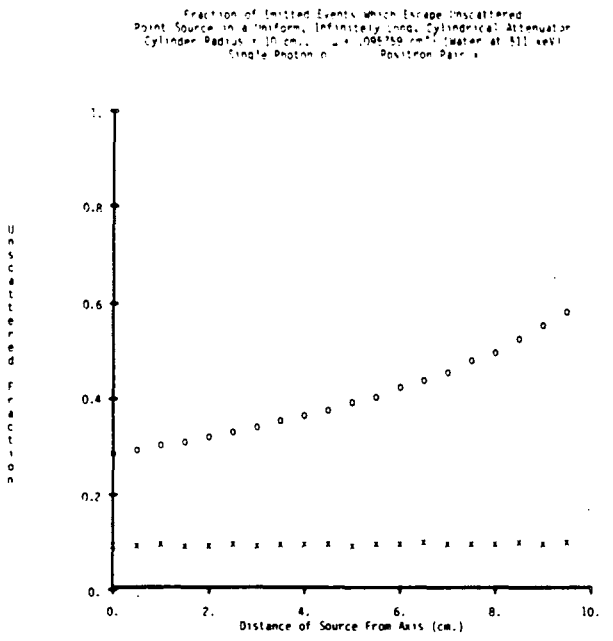

Figure 1.9 (a)

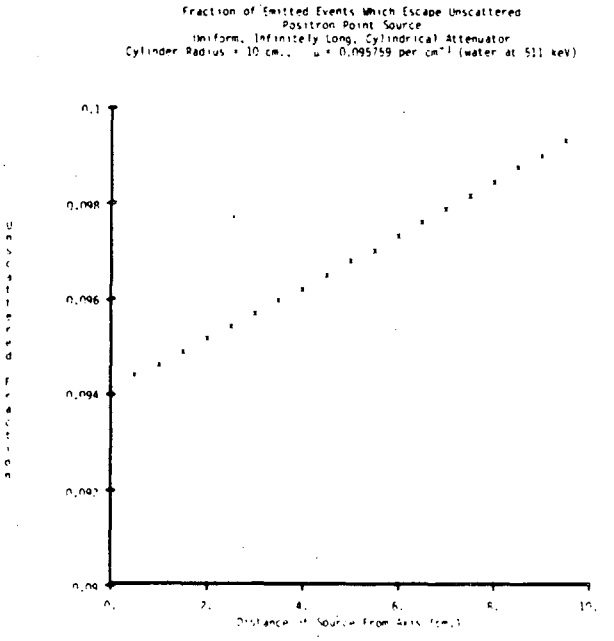

Figure 1.9 (b)

Fraction of events which escape unscattered from a uniform, infinitely long attenuating cylinder. The cylinder radius is 10 cm and the distance of the source from the cylinder axis is shown on the abscissa. The attenuation coefficient is that of water at 511 keV. In part (a), single photon and PET curves are shown on the same scale. In part (b), the PET curve is shown on an expanded scale.

placed counts will, in fact, be amplified by the attenuation correction which the scattering itself necessitated. The remainder of this work will therefore be concerned with the detailed assessment of the scatter background's spatial characteristics.

SECTION 2 - SIMULATION METHODS.

2.1. Monte Carlo Techniques.

Having established the motivation for a detailed study of the behavior of scattered radiation in gamma-ray emission imaging, we turn now to a consideration of the methods which might be used to accomplish this study. Although experiments certainly provide the most reliable data on scatter behavior, the amount of information which can be extracted from these studies is limited by several practical considerations: physical effects other than scattering contribute to the measurements that are made, the sources of radiation are expensive, unwieldy and sometimes dangerous to handle, and the wide variation of detection system parameters can be accomplished only at great expense.

In this work, Monte Carlo methods are used to simulate, using computers, the transport of photons through tissue. This sort of simulation occurs on a microscopic level. Photons are generated individually, "tracked" through various simulated interactions and then detected or discarded. A reasonably-accurate theory must exist which describes the microscopic behavior of each type of interaction to be simulated. This theory is used, as necessary, to make any stochastic decisions which may be required; computer-generated pseudo-random numbers are used to produce event distributions which conform to the theory of the process or interaction. In the simulation of Compton scattering, for example, outgoing photon directions must be distributed so that they agree with the Klein-Nishina collision cross sections.

In some cases, the method required to obtain the appropriate distribution is obvious. An example of such a situation is the generation of the direction of photons which are emitted from a radiation source. For sources in medical imaging, events are emitted uniformly in solid angle. Since solid angle is defined as the area subtended on a sphere of unit radius, two facts are apparent: 1) the solid angle subtended by a cone of photon flux of differential radius is independent of the cone's azimuthal orientation and 2) the cone, when rotated through the full 2π radians of azimuthal angle, will subtend a solid angle which increases as the cosine of its angle of inclination, θ. The proper distribution of photon directions can therefore be obtained if the azimuthal angle ϕ is distributed uniformly in the interval $[0,2\pi]$ and the cosine of the angle θ is distributed uniformly in the interval $[-1,1]$. Using two random numbers Λ_1 and Λ_2 uniformly distributed between zero and one we have

$$\phi = 2\pi\Lambda_1 \quad \text{and} \quad \theta = \cos^{-1}(2\Lambda_2-1) \quad . \tag{2.3}$$

For the generation of quantities whose distribution is non-trivial, a rigorous but fairly straightforward technique exists which is adequate for all the processes to be simulated in this work. This technique is referred to as cumulative inversion.

To apply the cumulative inversion technique, we must know a function, $f(s)$, of a random variable s, for which $f(s)\Delta s$ is the probability that the variable will assume a value within the small interval s to $s+\Delta s$. The function $f(s)$ is called a probability density function (PDF) of s. The cumulative density function (CDF) for the random variable s is defined as the probability that the variable will assume a value which

is less than or equal to some value of s. Thus the CDF is given by

$$F(s) = \int_{-\infty}^{s} f(s')\, ds' \quad . \tag{2.4}$$

F(s) is a random variable uniformly distributed between zero and one, so that s can be generated with the PDF f(s) if we can invert the function F. That is, if we use a pseudo-random number generator to generate Λ uniformly between zero and one

$$s = F^{-1}(\Lambda) \quad , \tag{2.5}$$

will generate s according to f(s).

2.2. Emulating the Physical Processes in Photon Transport.

2.2.1. Photon Free-Path sampling.

The probability density function for photon free travel in a material of constant linear attenuation coefficient, μ, is given by

$$f(r) = \mu e^{-\mu r} \quad . \tag{2.6}$$

$f(r)\Delta r$ is the probability that a photon will interact in the interval r to $r+\Delta r$ after having travelled from the origin without interaction. The cumulative density function for this PDF is given by

$$F(r) = \int_{0}^{r} \mu e^{-\mu r'} dr' = 1 - e^{-\mu r} \quad . \tag{2.7}$$

Denoting a pseudo-random number by Λ and using equation (2.5) we have

$$r = F^{-1}(\Lambda) = -\frac{1}{\mu} \ln(1-\Lambda) \quad . \tag{2.8}$$

The extension to nonuniform attenuators is accomplished by considering the random variable to be the normalized path length, u, given by

$$u = \int_0^r \mu(r')\, dr' \tag{2.9}$$

The PDF for u is

$$f(u) = e^{-u} \quad , \tag{2.10}$$

so that

$$F(u) = 1 - e^{-u} \quad , \tag{2.11}$$

and

$$u = F^{-1}(\Lambda) = -\ln(1 - \Lambda) \quad . \tag{2.12}$$

To find the distance, r, traveled before interaction, we must move along the path of the photon until the integral of equation (2.9) is equal to the generated value of u given by equation (2.10). For a uniform attenuator, $u=\mu r$, and equation (2.12) reduces to equation (2.8).

2.2.2. Determination of Interaction Type.

The selection of the type of interaction which will occur at a given interaction point is determined by the ratio of the different interaction cross sections. If the Compton and photoelectric attenuation coefficients of the material at the interaction point and at the inci-

dent energy are μ_c and μ_p, respectively, the probability that photoelectric absorption will occur is

$$P(\text{photo}) = \frac{\mu_p}{\mu_c + \mu_p} \quad , \tag{2.13}$$

while the probability for Compton scattering is 1-P(photo). The decision is made directly using a number Λ from the random generator. More specifically, if $\Lambda > P(\text{photo})$, the interaction is taken to be a Compton scatter; otherwise photoelectric absorption is assumed.

2.2.3. Sampling the Angular Distribution of Compton Scattered Photons.

The selection of the direction taken by a photon which emerges from a Compton scatter is accomplished through a straightforward application of the cumulative inversion technique. The probability density function in this case is a normalized form of the Klein-Nishina differential cross section for photon-electron scattering (1.7). For convenience, all energies are expressed with respect to the electron rest mass energy. Thus the energy of a photon, $h\nu$, is written as α where $\alpha = h\nu/m_0c^2$. Using this notation, (1.7) becomes

$$\frac{d\sigma}{d\alpha'} = \frac{\pi r_0^2}{\alpha^2} \left\{ \frac{\alpha'}{\alpha} + \frac{\alpha}{\alpha'} - 2\left(\frac{1}{\alpha'} - \frac{1}{\alpha}\right) + \left(\frac{1}{\alpha'} - \frac{1}{\alpha}\right)^2 \right\} \quad , \tag{2.14}$$

where r_0 is the classical electron radius, and α and α' are the incident and scattered energy of the photon.

To obtain the PDF we divide by the Compton total cross section, σ_c, so that

$$f_\alpha(\alpha') = \frac{1}{\sigma_c}\frac{d\sigma}{d\alpha'} \quad . \tag{2.15}$$

The CDF and its inverse are given by

$$F_\alpha(\alpha') = \int_{\alpha'_{min}}^{\alpha'} f_\alpha(\alpha'')\, d\alpha'' \quad , \tag{2.16}$$

and

$$\alpha' = F_\alpha^{-1}(\Lambda) \quad , \tag{2.17}$$

where Λ is is a pseudo-random number generated uniformly between zero and one. $\alpha'_{min}=\alpha/(2\alpha+1)$ is the minimum possible scattered photon energy. Equation (2.17) is solved numerically for regularly spaced values of the cumulative probability, Λ. This process is carried out for regularly spaced values of the incident photon energy, α. The calculations are tabulated, so that the result is a two-dimensional array of scattered photon energy, α', as a function of incident photon energy, α, and cumulative probability, Λ.

For computer simulations of Compton scattering, a pseudo-random number is generated and is taken as the cumulative probability Λ. Using Λ and the incident photon energy, α, a two-dimensional interpolation among four table entries is performed to deduce the outgoing photon energy, α'. The scatter angle can then be immediately obtained using the fundamental Compton relation given by

$$\cos\chi = 1 - \left(\frac{1}{\alpha'} - \frac{1}{\alpha}\right) \quad . \tag{2.18}$$

The azimuthal angle ω is uniformly distributed between zero and 2π radians and can therefore be obtained using

$$\omega = 2\pi\Lambda \tag{2.19}$$

where Λ is, once again, uniformly distributed between zero and one.

2.3. The Extent of the Computing Task.

The primary problem associated with the Monte Carlo methods just described is that computational costs can sometimes be prohibitive. In order to obtain an estimate of the practical limitations of these methods we consider briefly the extent of a typical scattering computation.

For simplicity, the source is taken to be a point in the center of an infinitely-long, water-filled cylinder with a radius of 10 centimeters. If N_i is the number of unscattered events to be obtained in the final image and f is the fraction of events which escape the attenuator unscattered into the solid angle of the detector, then N, the number of events which must be generated, is simply N_i/f.

The quantity f can be expressed as the product of two terms. In particular, if Ω_s is the solid angle subtended by the detector, then for a source which emits events uniformly into solid angle

$$f = \begin{pmatrix}\text{fraction of}\\ \text{events emitted}\\ \text{into } \Omega_s\end{pmatrix} \begin{pmatrix}\text{fraction of events}\\ \text{emitted into } \Omega_s \text{ which}\\ \text{escape unscattered}\end{pmatrix} \triangleq \frac{\Omega_s}{4\pi}\, p_{2e} . \tag{2.20}$$

Ω_s and p_{2e} are given by

$$\Omega_s = \int\int_{\text{detector}} \sin\theta \, d\theta \, d\phi \tag{2.21}$$

and

$$p_{2e} = 1/2 \int_{\text{detector}} \sin\theta \, e^{-2\mu R/\sin\theta} \, d\theta \quad . \tag{2.22}$$

If the detector is a ring system whose crystal radius is large compared to the slice thickness,

$$\Omega_s \cong 4\pi \tan^{-1}\left(\frac{1/2 \text{ gap}}{\text{crystal radius}}\right) \tag{2.23}$$

and

$$p_{2e} \cong e^{-2\mu R} \quad . \tag{2.24}$$

If the 1/2 gap is taken as 1 cm and the crystal radius as 50 cm,

$\Omega_s \cong .02$ steradians $\qquad f \cong 2.94 \times 10^{-4}$

$p_{2e} \cong .147 \qquad N \cong 340 \, N_i$

Thus if 30,000 unscattered events are required in the final image, 10^7 events must be generated.

For the computer code to be described below, approximately 2000 floating point operations are required per positron event. The simulation above would therefore require 3.5 minutes of processor time on a 100 MFLOP processor (1 FLOP = 1 floating operation per second) 35 minutes on a 10 MFLOP processor and almost 6 hours of processor time on a 1 MFLOP processor.

SECTION 3 - THE SIMULATION PROGRAMS.

3.1. Overall Structure.

The organization of the programs for the computer simulation of Compton scattering is shown in Figure 3.1. The programs can be adapted, with minor modifications, to simulate either positron emission or single-photon emission tomography. The emphasis in this and in succeeding sections will be on simulations of the former type.

Each square in Figure 3.1 represents one program, while each circle represents a set of intermediate or final results. The results most often exist physically as either a digital dataset on a magnetic storage medium or as printed text. Other forms of output, such as visual displays on color monitors and data plots are also important. The distributed structure of the package was motivated primarily by the extraordinary amount of computing required to simulate, with Monte Carlo techniques, the scattering of millions of individual photons.

The first program in the simulation system, and the eventual source of data for all subsequent processing, is a program called SMC. This program simulates the scattering of photons in a living subject. Its principle output is a list of photon histories which includes one entry for each photon that escapes the attenuator. The list is written to tape when the program concludes. Each entry contains information describing the photon's final position, direction, and energy, as well as the number of Compton collisions which it has survived. When data are generated

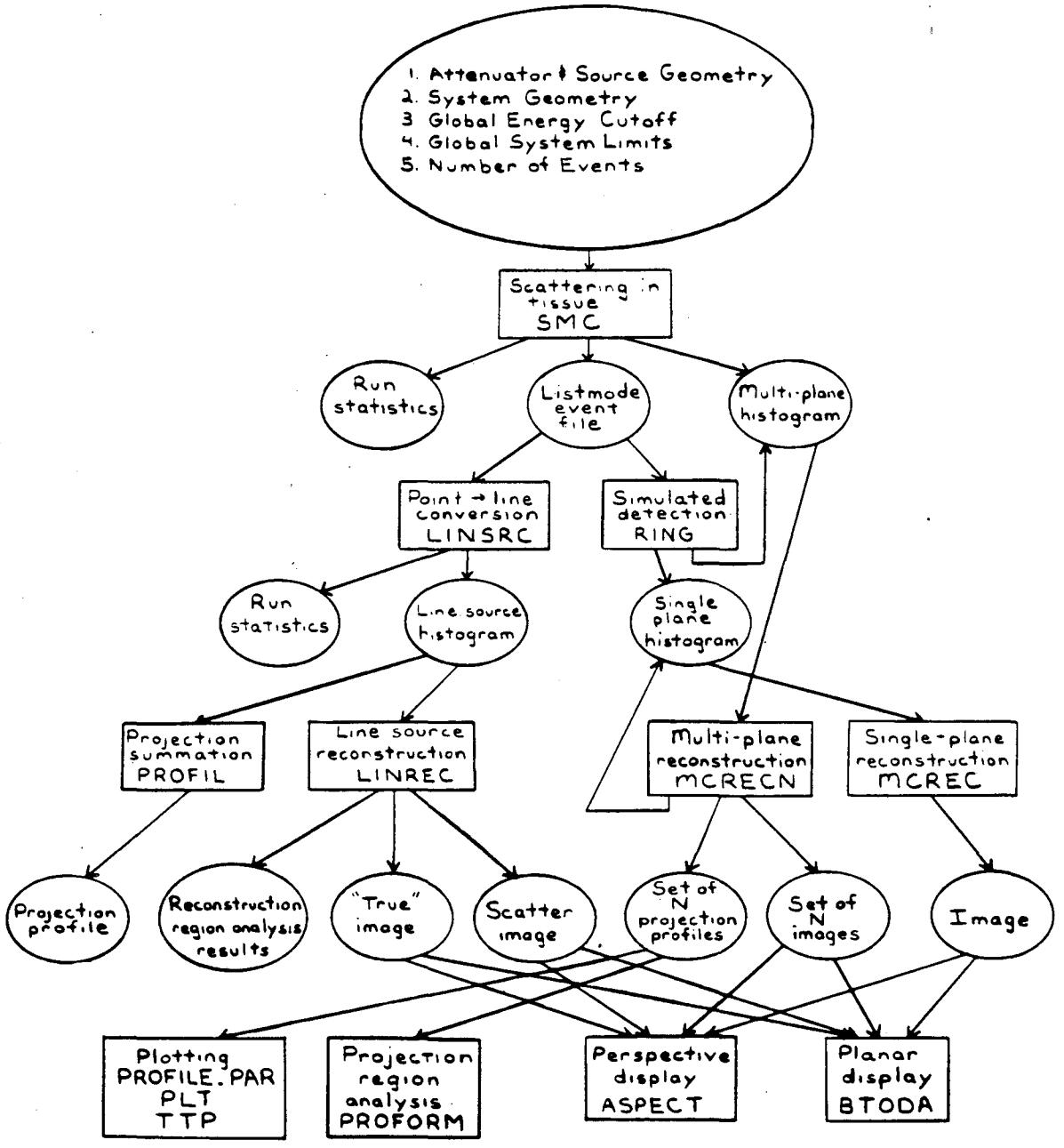

Figure 3.1

Organization of the scatter simulation programs.

in positron-mode, photon histories are written in pairs, and no entry is made unless both photonsescape the attenuator.

During event generation, SMC performs "real-time" event binning in multiple image planes. The result of this binning is a multi-plane histogram which is written to tape when the program is concluded. SMC also produces a few types of directly-useful results such as scatter histograms and separate scattering statistics for several classes of photons.

The next two levels in the computing hierarchy are composed primarily of programs which produce other detection-system histograms from the listmode output of SMC, or which reconstruct these histograms to produce an image. Examples in the first category are the program LINSRC which performs a weighted transformation of point-source events into a line source dataset and RING, which can be used to simulate a wide variety of positron ring system geometries. Reconstruction programs are LINREC, MCREC and MCRECN. The tasks performed by these programs are shown in Figure 3.1.

Output formatting, plotting, and interactive visual display programs complete the package. Example outputs from most of these routines can be found in Section 4.

3.2. Detailed Code Description.

In this section, the code for a few of the programs shown in Figure 3.1 is described in some detail. The code described is that which is of scientific interest. Not included are the binning and reconstruction

programs which include some interesting, but previously published, geometrical calculations.

3.2.1. Photon Scattering in Tissue - SMC.

SMC is a program which uses Monte-Carlo methods to simulate the scattering of photons in an arbitrary attenuating medium. It produces three types of output: scattering statistics, a listmode set of photon histories, and a histogram of detected events.

Figure 3.2 is a diagram of SMC structure and function. The first step in the program's execution is the initialization of major run-control variables, the most important of which are shown in Box 1. NTOT is the number of positron events to be generated, and its value must be selected so that it is small enough for reasonable program cost and output storage consumption, but large enough so that reasonable counting statistics can be achieved in images from simulated detection systems which use the SMC output. In order to partially relax the latter constraint, the program has been designed so that it stores enough information about the random number generation sequence so that it can be re-started where a previous job has left off.

A global energy minimum, EMIN, is used in a further effort to reduce computing costs. When the energy of any photon is reduced (in a Compton scatter), to less than this value, the photon's history is terminated. EMIN is usually set to be less than the photo-peak energy cutoff of any detector material of interest. An energy cutoff of 250 KeV is typical. In addition to the energy minimum, a set of limiting detec-

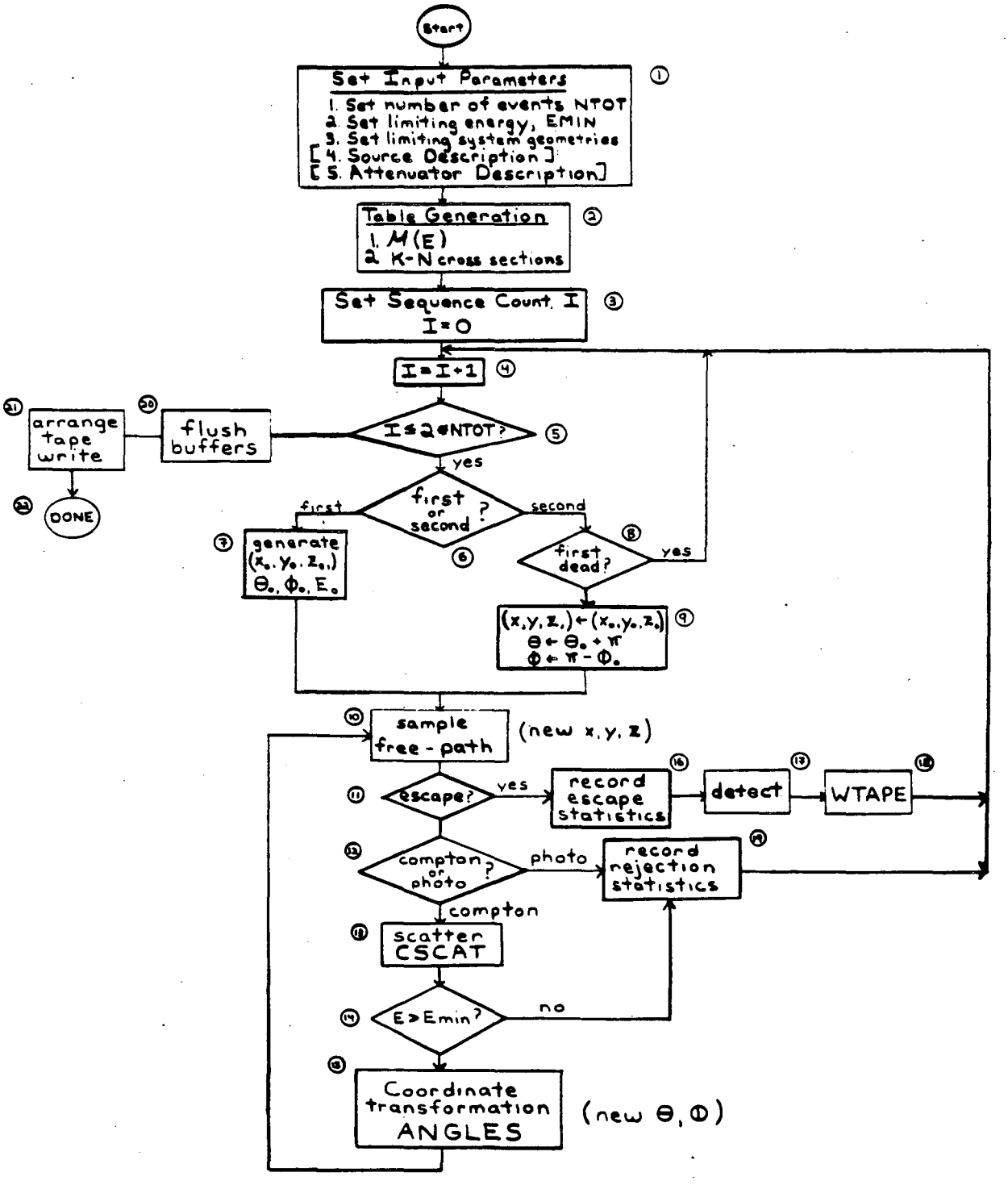

Figure 3.2

Detailed flow diagram for tissue scattering program, SMC.

tor geometries is used to reduce the amount of output data. The history of a photon which escapes the attenuator with an energy greater than EMIN is written to the listmode file only if the photon is detectable by some system whose geometry is within these limits. For a positron ring system, for example, one might require that any listmode event be detectable by some system with a crystal radius between 15 and 50 cm, and an axial coverage of 10 cm or less.

The program input parameters also include a description of the radiation source, and a description of the attenuator. This description is effected when appropriate event generation and free path sampling routines are linked to the main program after compilation. Sources which have been simulated range from a simple point source to a complex hot-spot phantom. For complicated source geometries, Monte Carlo techniques must be used to determine the point of origin for each event, while for a simple geometry like a point source only the initial direction is randomly distributed.

Attenuator geometries also vary in complexity. Simple attenuators which have been used very frequently include a uniform, water-filled circular cylinder of infinite length, and a uniform, infinitely long, water-filled elliptical cylinder. A free-path routine has also been written which samples an arbitrary arrangement of elliptical attenuators.

Before event generation and scattering is initiated, a few more initialization steps must be performed. These are shown in Box 2. First, for free path sampling, a table of the linear attenuation coefficients

for each material used in the attenuator must be generated over a certain energy range. The range might be from 250 to 520 KeV in 1 Kev increments. Second, a two-dimensional table derived from the Klein-Nishina cross sections must be generated by numerical integration. The principle behind this integration is described in Section 2.2.3, and the structure and use of the table are described below.

The actual scattering section of the code consists of a pair of nested loops, as shown in Figure 3.2. The outer loop (boxes 4-18) initiates, updates, and then completes the history of one photon. It consists of initial position and direction generation followed by scattering and disposal. The scattering of one photon is accomplished in the inner loop (Boxes 10-15), while disposal (consisting of detection, accumulation of run statistics, and output file maintenance) occurs in Boxes 16-19. The index for the outer loop is called "I" in Figure 3.2 and is incremented once for each photon. Initial position and direction are selected randomly for "first" photons in a positron pair, and derived, for "second" photons, from the first photon's position and direction values as shown in Box 9. To save computing time, second photons are not generated for positron events in which the first photon is absorbed in a photoelectric event, or in which the first photon's energy scatters below EMIN.

With its initial position and energy determined, a photon enters the inner loop for scattering. The first step in this process is the identification of the position at which the photon will interact. This task is performed by a free-path sampling routine for a specific attenuator as described above. Box 10 represents such a routine.

Although the details vary for different attenuator geometries, a basic procedure at this point is always observed: a random number between zero and one is generated which describes the distance travelled as a likelihood of occurrence. Small numbers indicate an unlikely event, namely the travel of the photon for a great distance through the medium without interaction. The exact relationship between the distance travelled and the cumulative probability, Λ, is derived from the exponential photon-flux relation

$$I/I_0 = \prod_{i=1}^{n} \exp(-\mu_i \Delta r_i) = \exp(-\sum_{i=1}^{n} \mu_i \Delta r_i) \quad . \tag{3.1}$$

Where I_0 is the initial intensity of a photon beam, I is the emerging intensity, μ_i is the total linear attenuation coefficient in material i, Δr_i is the distance travelled in material i, and n is the number of materials. For pixelized distributions of attenuation coefficients (e.g., from a transmission scan), Δr_i may be as short as the distance across one pixel. A uniformly distributed random number $\Lambda \in [0,1]$ is generated and $\{\Delta r_i\}$, i=1,2,...,n must be found such that

$$\Sigma \mu i \Delta r i = -\ln(1-\Lambda) \tag{3.2}$$

The free-path routine uses the knowledge of the attenuation coefficient in each material and the position of the material boundaries to solve for $\Delta r = \Sigma \Delta r_i$ in terms of Λ and $\{\mu_i\}_{i=1,n}$. A new photon position (x,y,z) follows directly from Δr.

When the photon moves to its new position it will either escape the attenuator or interact in some way. Photons which escape take the branch at Box 11 that leads to final processing in Boxes 16-18, whose functions

will be discussed below. A random number, Λ, is generated for photons which do not escape in order to determine the type of interaction that occurs. If Λ is such that

$$\Lambda < \frac{\mu_p(E)}{\mu_p(E) + \mu_c(E)} ,$$

then a photoelectric event is assumed. In the inequality above, μ_p is the photoelectric linear attenuation coefficient of the material at the interaction point at energy E, and μ_c is the Compton attenuation coefficient. If photoelectric absorption occurs certain information is stored, as indicated in Box 19, and the event is terminated. If Λ does not meet the requirement above, the interaction is assumed to be a Compton scatter and the processing in Box 13 occurs.

The function of Box 13 is the determination of a new energy and direction for the Compton-scattered photon. The relative photon direction is uniquely defined by the polar scattering angle, χ, and the azimuthal scattering angle, ω. To produce the two scatter angles, CSCAT (the routine represented by Box 13) derives the outgoing energy by using a table lookup followed by a two-dimensional interpolation. The axes of the table are the initial energy and the value of a generator-produced number Λ. The fundamental Compton equation yields the polar scattering angle, χ, directly from the new energy. The azimuthal scattering angle, ω, is generated uniformly between zero and 2π radians.

At this point, the photon being scattered is again checked for viability. If the energy resulting from the Compton scatter is less than EMIN, the event is discarded, statistical information is recorded, and a

new event history is initiated. If, on the other hand, the new energy is greater than EMIN, the scatter angles χ and ω are transformed into the standard angles θ and ϕ at Box 15, and the history is continued with a new sampling of the free path length. Thus photons entering the scattering loop continue scattering until they escape the attenuator, are absorbed in a photoelectric event, or are energetically attenuated below the energy baseline in a Compton interaction.

Photons which escape the attenuator are further processed in Boxes 17 and 18. Box 17 represents binning by the detection system. This binning, which occurs in multiple image planes, is usually kept simple. There are, for instance, no scatter shields used in the simulation of a PET ring system. This is done because detection-system binning, as shown in Figure 3.1, is superfluous to the function of SMC: the listmode data set can be processed separately at a later time to produce the same results. It is useful, however, as a means of verification for the event-generation portion of the code.

In a typical detection simulation, photons simply strike a solid annulus of detector material such as BGO, penetrate it exponentially, deposit energy, and are detected. The crystal penetration is modeled as a simple monte carlo free-path length sampling of the type described by equation (2.8) where mu, in this case, is the total linear attenuation coefficient of the detector material at the photon's energy. If the free path length so obtained is greater than the distance to the rear boundary of the detector annulus, the photon escapes and no event is recorded. Otherwise a photoelectric absorption occurs and the event is recorded on the chord corresponding to the crystal which contains the

point of interaction. Implicit in this procedure is the (not altogether realistic) assumption that the photoelectric linear attenuation coefficient, τ, of the detector is much greater than the Compton attenuation coefficient, σ.

The cylindrical detector annulus is logically divided along its axis into image planes and around its circumference into discrete crystals. Events in each plane are binned separately by chord to make a histogram suitable for reconstruction, and events in each plane are are also binned according to the number of scatters for each photon. Symmetry in this latter histogram is an important check on program function. An example set of scatter histograms for a central point-source binned by a 5-plane system is shown in Table 3.1. Note that only the central image plane contains any unscattered coincidences.

The listmode file is managed by a routine called WTAPE. For positron-mode simulation, WTAPE considers photons as pairs, but is called for each photon to simplify main program structure. When it is called for first photons, it simply copies history information into a small holding array. When the second photon arrives, the event is evaluated as a listmode file candidate. If the event may be detected by some system within the global limits (see above), a packing routine is called which allows the history information for both photons to be stored in 120 bits. These bits (which represent two 60-bit words on a CDC 7600) are temporarily stored in a large buffer array internal to WTAPE and transparent to the main program. When event generation ceases, the main program executes a WTAPE "flush call" during which any remaining buffer events are written to the listmode file. This is indicated in Box 20.

SCATTER HISTOGRAMS BY IMAGE PLANE

PLANE 1 OF 5, CENTERED AT Z= 0. CM.

SCATTERS BY FIRST PHOTON \ SCATTERS BY SECOND PHOTON	0	1	2	3	4	5	6	7 OR MORE
0	30003	532	119	12	5	0	0	0
1	519	284	86	9	1	0	0	0
2	103	71	25	6	0	0	0	0
3	14	17	2	0	1	0	0	0
4	0	0	0	0	0	0	0	0
5	0	0	0	0	0	0	0	0
6	0	0	0	0	0	0	0	0
7 OR MORE	0	0	0	0	0	0	0	0

PLANE 2 OF 5, CENTERED AT Z= 2.00 CM.

SCATTERS BY FIRST PHOTON \ SCATTERS BY SECOND PHOTON	0	1	2	3	4	5	6	7 OR MORE
0	0	1086	224	38	5	0	0	0
1	1009	519	127	29	3	0	0	0
2	230	160	54	6	2	0	0	0
3	39	28	6	1	0	0	0	0
4	7	4	1	0	0	0	0	0
5	0	0	0	0	0	0	0	0
6	0	0	0	0	0	0	0	0
7 OR MORE	0	0	0	0	0	0	0	0

PLANE 3 OF 5, CENTERED AT Z= 4.00 CM.

SCATTERS BY FIRST PHOTON \ SCATTERS BY SECOND PHOTON	0	1	2	3	4	5	6	7 OR MORE
0	0	957	203	31	2	0	0	0
1	971	533	136	20	6	1	0	0
2	236	141	39	10	2	0	0	0
3	30	28	6	1	0	0	0	0
4	7	4	0	1	0	0	0	0
5	0	0	0	0	0	0	0	0
6	0	0	0	0	0	0	0	0
7 OR MORE	0	0	0	0	0	0	0	0

PLANE 4 OF 5, CENTERED AT Z= 6.00 CM.

SCATTERS BY FIRST PHOTON \ SCATTERS BY SECOND PHOTON	0	1	2	3	4	5	6	7 OR MORE
0	0	910	209	31	2	0	0	0
1	950	463	140	29	2	0	0	0
2	218	108	43	5	1	0	0	0
3	40	29	8	0	0	0	0	0
4	4	3	0	1	0	0	0	0
5	0	0	1	0	0	0	0	0
6	0	0	0	0	0	0	0	0
7 OR MORE	0	0	0	0	0	0	0	0

PLANE 5 OF 5, CENTERED AT Z= 8.00 CM.

SCATTERS BY FIRST PHOTON \ SCATTERS BY SECOND PHOTON	0	1	2	3	4	5	6	7 OR MORE
0	0	785	219	34	6	0	0	0
1	822	426	111	26	1	0	0	0
2	190	123	37	5	1	0	0	0
3	36	16	5	1	1	0	0	0
4	1	4	0	0	0	0	0	0
5	0	0	0	0	0	0	0	0
6	0	1	0	0	0	0	0	0
7 OR MORE	0	0	0	0	0	0	0	0

Table 3.1

Results of SMC event binning for a positron point source at the center of a 20 cm uniform attenuating cylinder. The detector system is a ring with a 90 cm crystal radius, 280 crystals, 5 image planes and no inter-plane scatter shielding.

When listmode file writes are completed a routine called ASMCCS is called which generates system directives that cause the file to be written to tape along with some naming information. The naming information uniquely identifies the source, attenuator, number of events generated, the photon sequence number "I" at job termination (this is a stochastic variable), and the energy cutoff EMIN. This processing is represented by Box 21.

The program's remaining output, which consists of the detection-system histogram and the run statistics accumulated in boxes 16 and 19, must also be disposed of at job termination. The histogram array is written to a file by WTAPE and a unique tape pathname and system directives are generated by ASMCCS. The run statistics are printed on the output text file. An example output is shown in Table 3.2 for a positron run of 10^7 raw events for a point source in the center of a uniform, water-filled, circular cylinder of infinite axial extent. For this particular simulation, photoelectric absorption was disabled.

3.2.2. Point to Line Source Conversion - LINSRC.

LINSRC is a program which operates on the listmode output of SMC to convert point source simulation results into simulation results for a source distributed along the line $x = x_S$, $y = y_S$ where (x_S, y_S) are the x-y coordinates of the point source. Implicit in the logic of the program is the assumption that the attenuator in the point-source simulation is cylindrically symmetric and that the axis of the attenuator's symmetry lies along the axis of rotation of the tomograph. It is also assumed that the attenuator and the line source have an

```
        $$$$$$$ RUN TOTALS $$$$$$$

   15728991 PHOTONS WERE GENERATED TO SIMULATE 10000000 POSITRON EVENTS.

     RESULTS FOR FIRST PHOTONS
10000000.00 FIRST PHOTONS WERE GENERATED.
 5728992.00 FIRST PHOTONS ESCAPED THE ATTENUATOR, FRACTION OF FIRST PHOTONS= .5729.
 4271008.00 FIRST PHOTONS SCATTERED BELOW THE ENERGY BASELINE, FRACTION OF FIRST PHOTONS= .4271.
 2878948.00 FIRST PHOTONS ESCAPED WITHOUT SCATTERING, FRACTION OF FIRST PHOTONS= .2879.

     RESULTS FOR SECOND PHOTONS
 5728992.00 SECOND PHOTONS WERE GENERATED.
3373855 .00 SECOND PHOTONS ESCAPED THE ATTENUATOR, FRACTION OF SECOND PHOTONS= .5889.
 2355137.00 SECOND PHOTONS SCATTERED BELOW THE ENERGY BASELINE, FRACTION OF SECOND PHOTONS= .4111.
 1751118.00 SECOND PHOTONS ESCAPED WITHOUT SCATTERING, FRACTION OF SECOND PHOTONS= .3057.

     RESULTS FOR SINGLE PHOTONS
 9102847.00 PHOTONS ESCAPED THE ATTENUATOR.
 6626145.00 PHOTONS WERE TRAPPED BY THE ATTENUATOR.
           MEAN NUMBER OF SCATTERS FOR ESCAPING PHOTONS=  .6773.
           MEAN NUMBER OF SCATTERS FOR TRAPPED PHOTONS= 1.7038.

     RESULTS FOR POSITRON EVENTS.
       0.   EVENTS WERE ABSORBED PHOTOELECTRICALLY.
    3373855 EVENTS HAD BOTH PHOTONS ESCAPE.
    2087008 EVENTS WERE REJECTED IN LISTMODE TAPE WRITE.
          0 EVENTS WERE REJECTED BECAUSE OF PACKING RANGE ERRORS.
           MEAN TOTAL SCATTERS ASSCOIATED WITH ONE POSITRON EVENT= 1.1097.
```

Table 3.2

SMC run statistics for the simulation of Table 3.1.

infinite axial extent.

To accomplish the line source conversion, LINSRC sequentially reads the listmode file and assigns to each point source event a line source weight which depends on the detector geometry. For a positron ring system, the weight is a real number between zero and the slice thickness. With this weighting scheme, a doubling of the slice thickness causes a fourfold increase in the number of unscattered events detected. This is realistic since a doubling of the slice thickness doubles the source length which lies within the field and (to a very close approximation) doubles the solid angle subtended by the detector.

Each point source event is considered as an infinitesimal source at all points along the line of the source to be synthesized. At each location, it emits radiation only along the final flight paths of its two photons. Point source events which emit detectable radiation at a large number of locations are assigned large line source weights and those which emit very little detectable radiation are assigned small weights. The actual weight for an event is calculated as the intersection of two intervals. One interval is derived from each of the event's two photons. The interval for one photon is the set of positions along the source line from which that photon can be emitted to move along its direction of flight to hit the scintillation crystals without hitting the scatter shields. The calculation of a line source weights is illustrated in Figure 3.3.

Events with nonzero weights are binned to form a sinogram for the particular detection system being simulated. If desired, events can be binned separately for different numbers of scatters. In this way ,an image of, say, single scattered events for a particular source, attenuator and detection system can be created. Many of the results in Section 4 are derived from sinograms produced by LINSRC and a number of tables have been included which show the number of events detected as a function of the number of scatters for each photon.

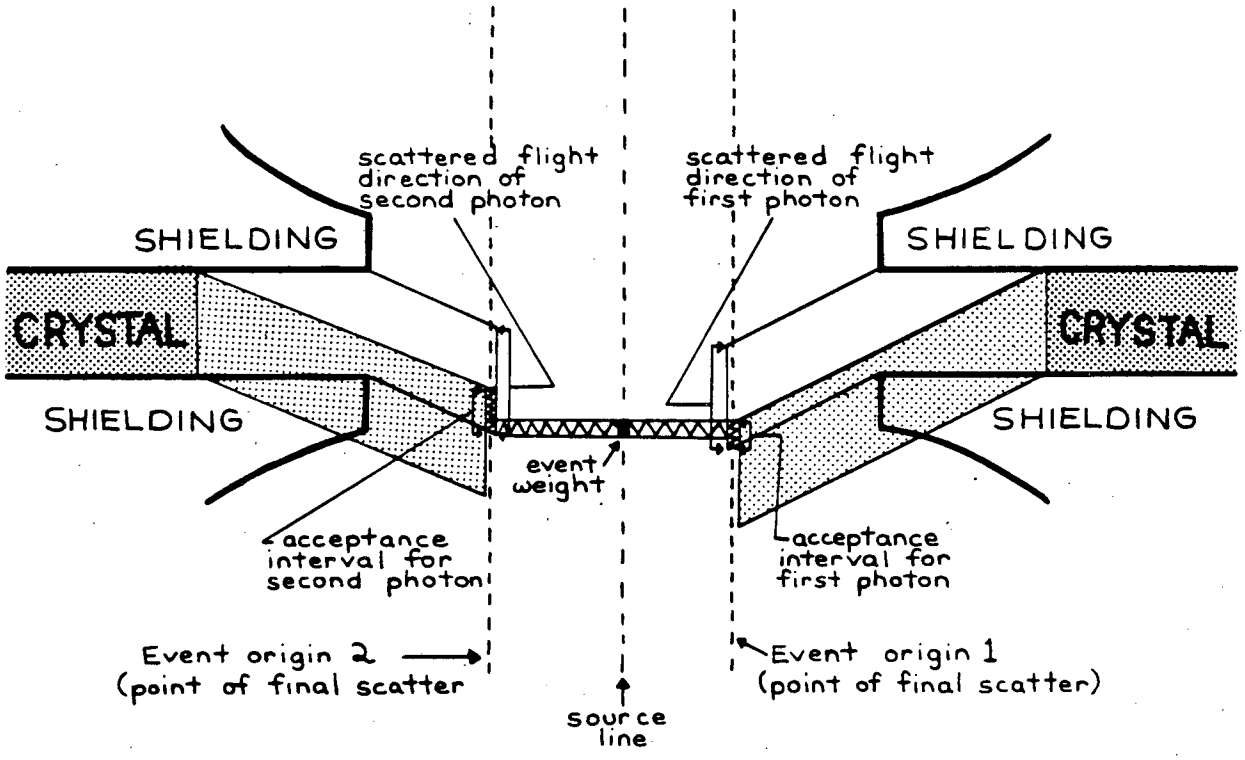

Figure 3.3

Calculation of a line source weight from a positron point source event. The shaded region along the source line constitutes the set of locations from which both photons can reach the crystals without striking the scatter shields.

SECTION 4 - SIMULATION RESULTS.

4.1. Uniform Cylindrical Attenuator With a Central Source.

Figures 4.1 through 4.8 show various outputs derived from tissue scattering simulations for a line source along the axis of an infinitely long cylinder filled with water. In some simulations, the attenuator diameter is 20 cm, and in others it is 30 cm. With the source along the axis of the attenuator, the source/attenuator combination is cylindrically symmetric so that when the combination's axis lies along the axis of rotation of a tomograph, all angular views are equivalent. In fact, a symmetry exists within any single projection: If bin_j is the central bin in a projection, bin_{j+n} is equivalent to bin_{j-n} for all integers n.

4.1.1. Logarithmic Plots of Composite Projections.

Figures 4.1 and 4.2 show the variation of scatter with the minimum energy required for photo-detection and with slice thickness. In Figure 4.1 the attenuator diameter is 20 cm and in Figure 4.2 it is 30 cm. Each curve in these figures is obtained by summing all the angles in a sinogram and then "folding" the result about the central bin to take advantage of the internal symmetry just described. This decreases statistical fluctuations in the data. The value of each bin in the final composite projection is thus the average of two bins which are equidistant from the center. The detection system is a simulated version of the Donner 280-Crystal Positron Tomograph[14]. A log scale has been used on the abscissa because the number of unscattered events is approximately three orders of magnitude greater than the number of scattered events. This is

largely due to the very deep scatter shields of the simulated detector. These data have not been corrected for attenuation. Both the 20 cm and 30 cm results are shown on the same scale, and the total numbers of events in the two cases are similar because 50 per cent more raw events were generated for the 30 cm simulation.

The curves in Figures 4.1 and 4.2 are remarkable mostly because of their similarity. With the exception of the reduction in the number of events that occurs with a larger attenuator, the shape of the scatter background appears to be only a very weak function of the attenuator diameter.

The curves in Figures 4.3 through 4.6 are of the same type as those in Figures 4.1 and 4.2. Figures 4.3 and 4.4 emphasize the energy variation of the scatter background. Again, the 20 cm and 30 cm curves are very similar. It should be noted that even with an energy cutoff of 500 KeV, the scatter background is not significantly affected in the region surrounding the source (recall that the initial photon energy is 511 KeV).

Figures 4.5 and 4.6 emphasize the variation of the scatter background with slice thickness. Figures 4.5(b) and 4.6(b) are scatter histograms of the type shown in Table 3.1. They have been included to show that the effect of varying the slice thickness differs for scattered and unscattered events. In particular, the number of unscattered events varies directly in proportion to the solid angle subtended by the detector (i.e. with the slice thickness) and with the length of the source in the field. The variation in the number of scattered events is more complex. For the case of the 20 cm attenuator (Figure 4.5), the

transition from a half-gap of 1.5 cm to one of 1.0 cm causes a decrease in the number of unscattered counts by a factor of 2.25 but decreases the scattered events by a factor of 3.3. For the change in half-gap from 1.0 to 0.5 cm, the effect is more dramatic. The unscattered events, as expected, are diminished by a factor of 4, while the scattered events are reduced by a factor of 8. Very dramatic gains in reduction of the scatter background amplitude are therefore possible in high-dose imaging or with imaging agents with very short half-lives. It is only in these situations, of course, that the geometric decrease in the number of unscattered image-forming events can be tolerated.

It is also worth noting that the width of the scatter background does not increase appreciably with an increase in the slice thickness at a constant energy cutoff even though the acceptance angle of the shields is greater.

4.1.2. The Effect of Attenuation Correction.

Figure 4.7 shows the effect of attenuation correction on the results of the 20 cm simulations of the previous section. For comparison with the figures above, the composite projection for 300 KeV with a half-gap of 1 cm is shown in parts (a) and (b) on a logarithmic scale before and after correction. The same projection is shown in (c) and (d) on a linear scale. To make this possible, the unscattered events in the central bin have been removed.

The shape of the curve in (d) is a measure of the validity of the approximation that the scatter background is approximately constant in reconstruction. If this were true, the scatter would be semi-circular in

profile after attenuation correction. We see from the figure that this a rather crude approximation.

4.1.3. Regional Scatter Fraction Analysis.

Figure 4.8 shows the fraction of the total number of events which lie outside a central region of varying size in projection. This fraction is shown separately as a function of energy cutoff, half-gap and attenuator radius in parts (a)-(c), respectively.

The procedure used to create the graphs can be explained as follows: For the simulation of interest, all projection angles are added and the result is folded as described above to obtain a composite projection containing all of the events in the sinogram. A series of successive regions in this projection is then analyzed. More specifically, the number of events which lie outside each region is determined and this number is divided by the total number of events in the projection to obtain one point on one of the curves in the figure. In all cases, the first region is the central bin. The second region is the central bin and its two neighbors, the third region is the second region augmented by its two neighboring bins, etc. For each region, the value derived is plotted on the ordinate versus the distance of (either of) the region's edge bins from the center of the projection. Thus, for the first region, the distance from the center is zero. For the second, the distance is one, and so on. One curve is dotted in each part of the figure to emphasize the fact that this curve is common to all three parts.

4.2. Uniform Attenuator With Non-Central Source.

With the loss of the cylindrical symmetry associated with a central source, the analysis and display of results becomes much more difficult. Angles can no longer be sensibly added with the result that two orders of magnitude more events would have to be generated in order to obtain projection plots with a bin-to-bin variance like those above. The computing effort for this approach is prohibitive. Analysis of the data in reconstruction is also not possible. This can be deduced from the figures in the previous section, wherein the number of events in bins containing scattered data is never more than a few hundred counts. Since each composite projection represents the sum of 140 angles, it can be seen that few projection bins in the original sinogram contain more than one or two events.

Because of these difficulties, the results for simulations using off-center line sources are shown in Figure 4.9 and 4.10 without further processing. Each frame in one of the figures is a sinogram from one simulation. The grey scale in the pictures is linear and the brightness in the unscattered bins is severely "clipped". In both figures, the attenuator radius is 10 cm, but in Figure 4.9 the location of the source is (5,0,0), or half-way to the edge along a radius, while in Figure 4.10 the source location is (9.5,0,0). Because the simulated detector is a positron ring system, the angular range for each sinogram is from zero to π radians.

In some respects, the scattered events behave similarly to those in the central source simulations: The width of the background is fairly

insensitive and the amplitude fairly sensitive to changes in the half-gap, while the width and amplitude are both sensitive to changes in the energy cutoff.

The off-center simulations are remarkable, however, because they strongly emphasize one point that is easily overlooked in the simulations of the previous section: in PET imaging, the scatter background is not contained by the attenuator as it is in single photon imaging. In fact, for low energy cutoffs, there appears to be some "bunching" of events at the edge of the patient port, at least 20 cm from the edge of the attenuator. The fact that a large number of scattered events appear outside the attenuator might be very useful in the design of correction algorithms which could get an estimate of the scatter background by sampling the sinogram in areas known to contain no source.

4.3. Conclusions and Suggestions for Further Work.

The goal of the research presented in this thesis was the development of a set of computer simulation programs useful in the design of new instrumentation and in the design and evaluation of correction algorithms. This has been accomplished, the methods described and a number of results presented.

The organization of the simulation programs is very efficient for the assessment of changes in the scatter background due to changes in tomograph design parameters. This efficiency is attributable mainly to extensive segregation of function; the output of the tissue scattering program, for example, is preserved as a list of photon histories which can be "acquired" by any number of simulated detectors at minimal expense. In fact, this feature was invoked to create the results of Sections 4.1 and 4.2, which were produced by the LINSRC program operating on the output list from SMC. In these figures, the variation in the distribution of scattered photons with attenuator radius, energy cutoff and slice thickness was presented. It was shown that changes in the slice thickness and the attenuator radius affect almost exclusively the amplitude of the scatter background, leaving the shape largely unchanged. Scattered events can be more easily attenuated by narrowing the slice gap than unscattered events, but unscattered events are attenuated by the square of the decrease in the width of the slice.

The effect of tomograph design parameters on the scatter background in projection could be almost completely characterized with a series of additional simulations that could be performed by the present programs.

In particular, the radius of the detector assembly and the radius of the scatter shielding should be varied separately, each for a succession of narrowly-spaced steps.

Several refinements could be made to the simulation programs to make them a more sophisticated tool for instrument design. More physical effects such as positron range and angulation can be added to the in-tissue phase of the simulation, and the simulation can be continued when the photons reach the detector. For the latter improvement, the currently-employed exponential gamma-ray penetration of crystals could be replaced by a Monte Carlo simulation of Compton scattering and photoelectric absorption in the crystals and scatter shields. The visible scintillation light emitted after absorption could be further scattered and dead time in the electronics could be simulated.

The results presented in the preceding sections will be used in the future as the basis for an iterative scatter correction algorithm. With the detector characteristics fixed, each sinogram corresponding to a particular attenuator size and source position will serve as an input data set for a maximum likelihood fit. The probability density function in such a fit will use the characteristics of the attenuator, the source position and the physical behavior of Compton Scattering to assign a likelihood of event detection to each location in the sinogram. The fixed-parameter functions obtained from the fits will constitute a computationally-efficient means of projecting scatter. These functions can then be used in the algorithm outlined below, which uses several iterations of the convolution reconstruction method to subtract scatter. At each step below, the "current" image is the updated estimate of the

true source distribution.

Scatter Correction Algorithm Outline

(1) Perform a standard reconstruction of the raw data with attenuation correction, and use the result as the initial estimate of the "current" image.

(2) Reproject the "current" image to predict the scatter background using the function obtained above and the measured attenuation distribution.

(3) Subtract the raw data from the projections of (2).

(4) If the subtracted projections of (3) are small compared to the statistical uncertainty of the raw data, STOP. The iterative procedure is complete, and the "current" image represents the true source distribution.

(5) Perform a standard reconstruction of (3) (with attenuation correction) to obtain an "error" image.

(6) Subtract the "error" image of (5) from the "current" image to obtain a new estimate of the "current" image.

(7) Go to (2).

The key to this approach is the fact that a standard reconstruction (without scatter correction) is a good first order estimate of the true source distribution, and that the first reprojection of (2) is a good approximation of the raw data plus the scatter background. This assumes

that the "scatter" portion of the reprojected scatter background is small. It is expected that this type of algorithm will converge in one or two steps.

Free-path sampling routines for arbitrary attenuators have already been written and tested. These will be used to extend the algorithm above and to increase our qualitative understanding of the effects of attenuator non-uniformities on the spatial distribution of Compton-scattered photons.

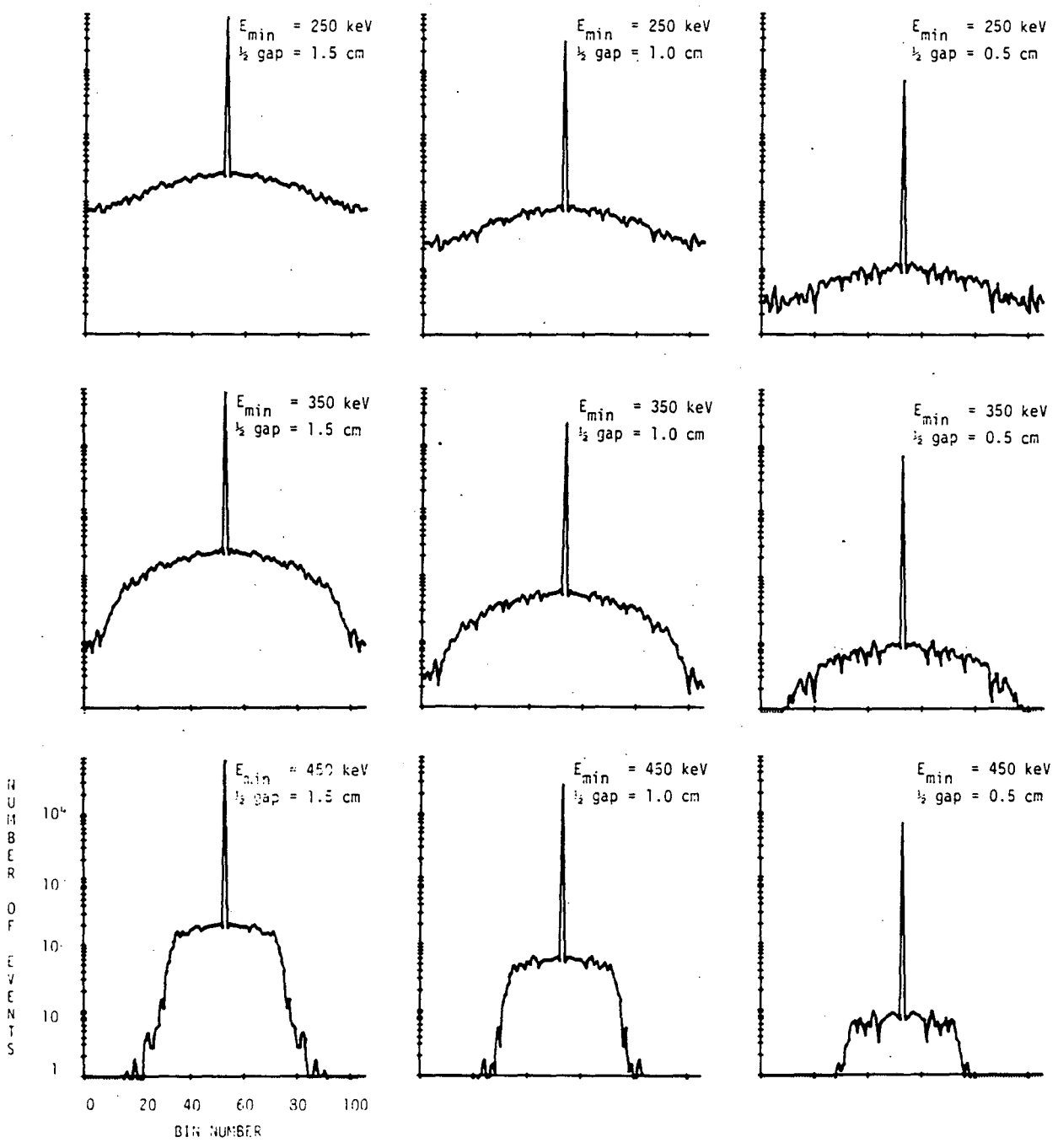

Figure 4.1

Logarithmic plot of scatter background in projection as a function of energy cutoff and effective slice thickness. The source is a central line parallel to the axis of a 20 cm uniform attenuating cylinder. Each curve is the sum of all angles from a simulated ring detector. The bin width is 0.552 cm.

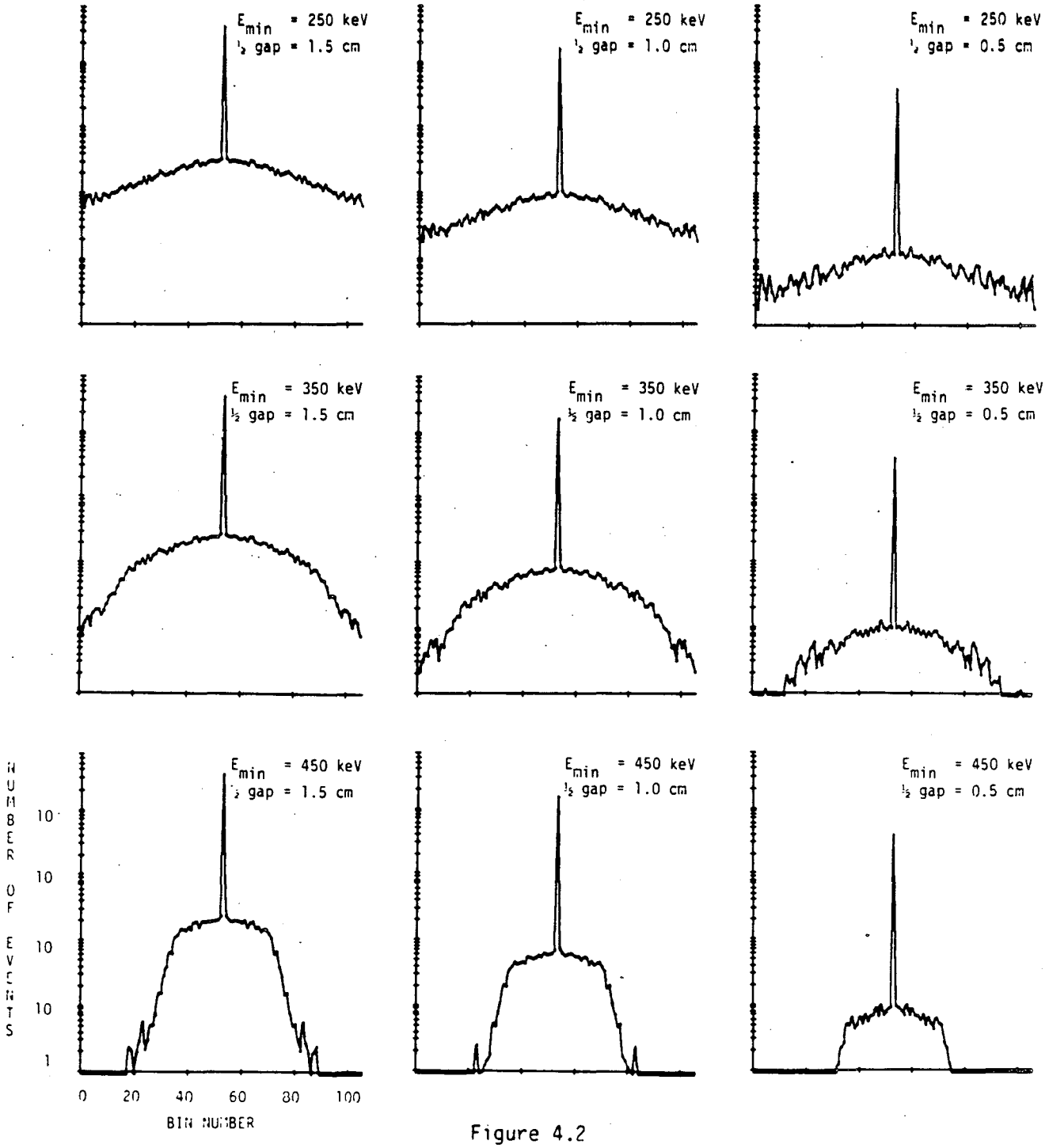

Figure 4.2

Logarithmic plot of scatter background in projection as a function of energy cutoff and effective slice thickness. The source is a central line parallel to the axis of a 30 cm uniform attenuating cylinder. Each curve is the sum of all angles from a simulated ring detector. The bin width is 0.552 cm.

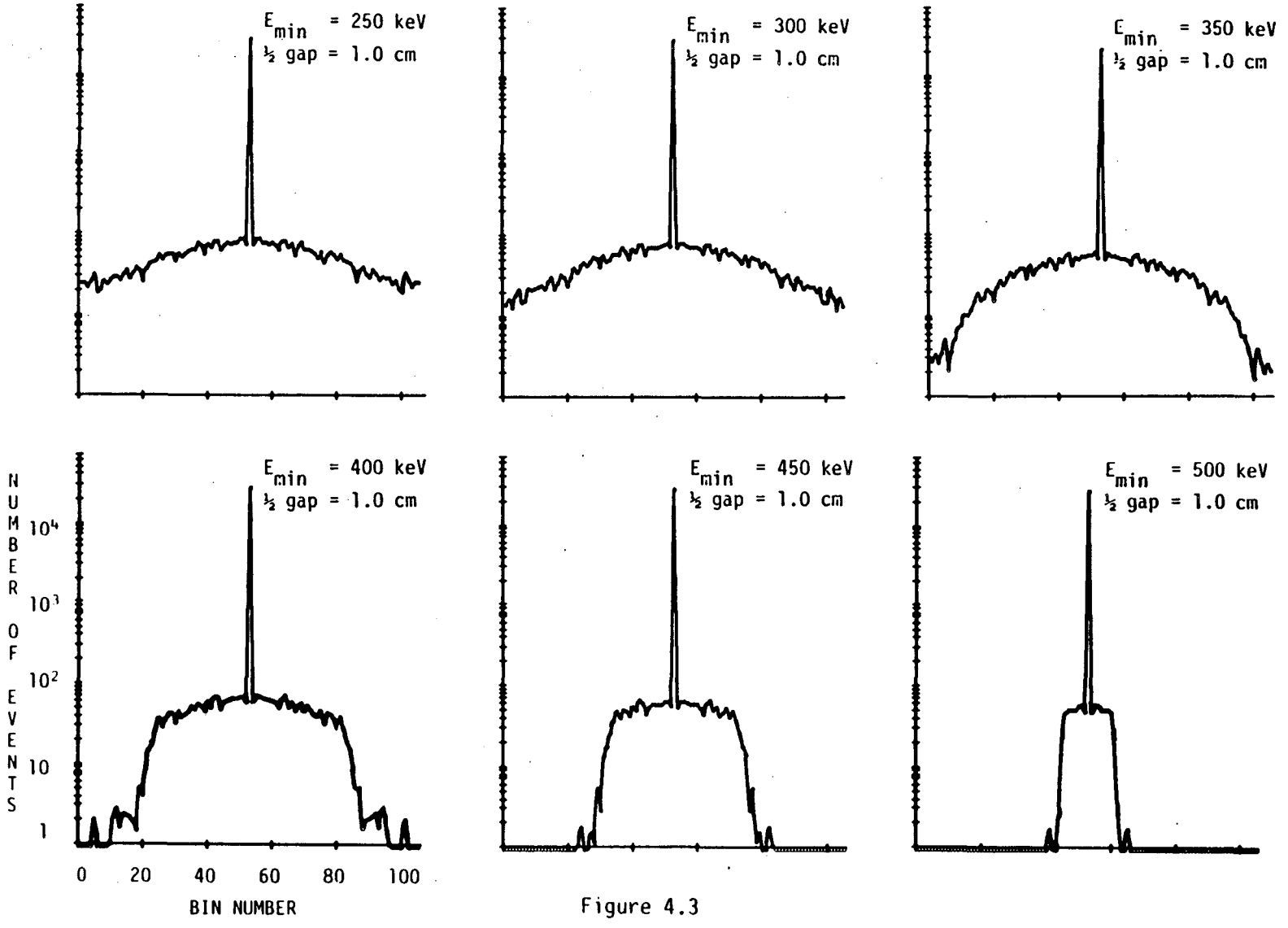

Figure 4.3

Logarithmic plot of the energy cutoff dependence of scatter background in projection. The source is a central line. The attenuator is a uniform, water-filled cylinder with a diameter of 20 cm and the shielding half-gap is 1.0 cm.

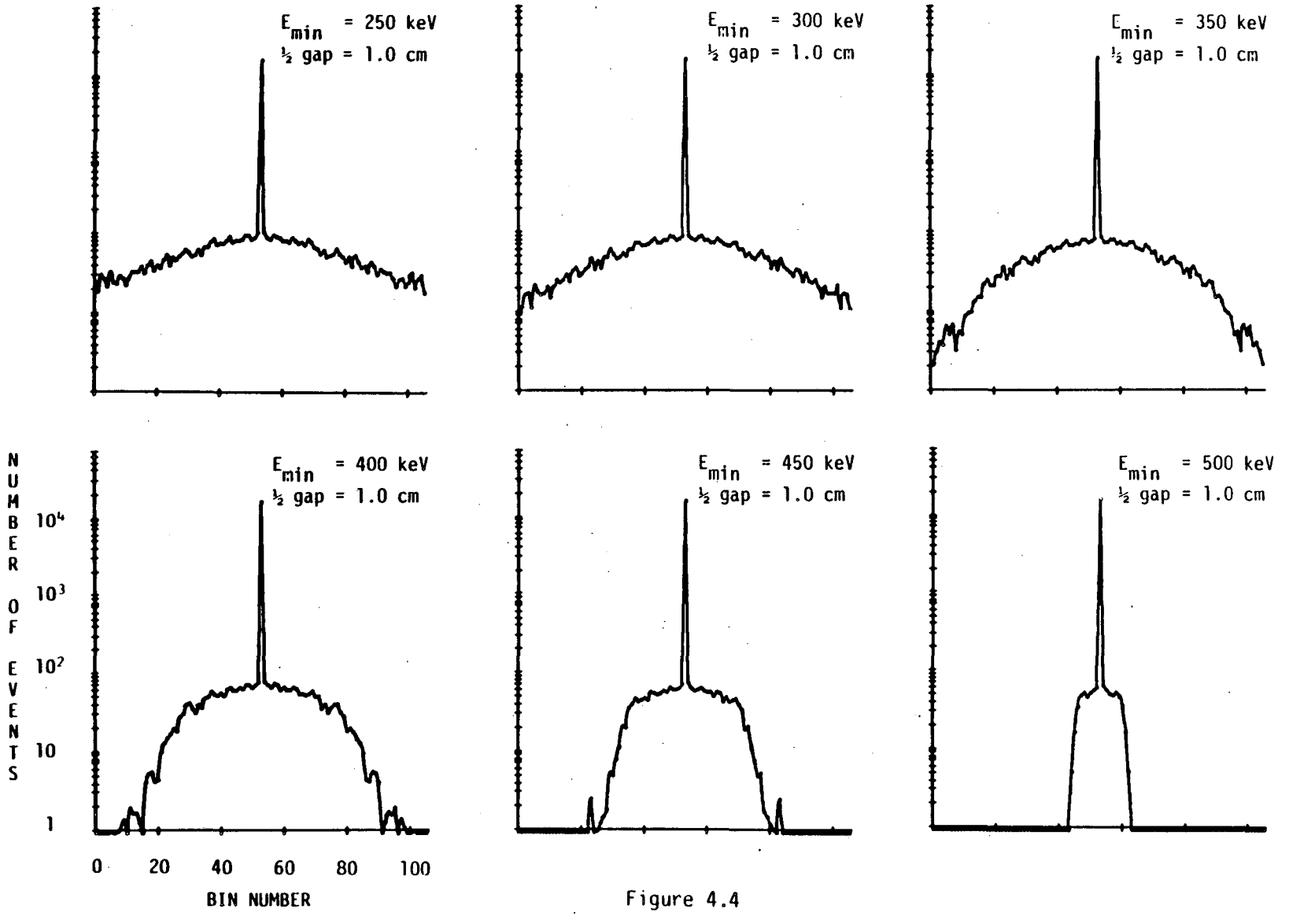

Figure 4.4

Logarithmic plot of the energy cutoff dependence of scatter background in projection. The source is a central line. The attenuator is a uniform, water-filled cylinder with a diameter of 30 cm and the shielding half-gap is 1.0 cm.

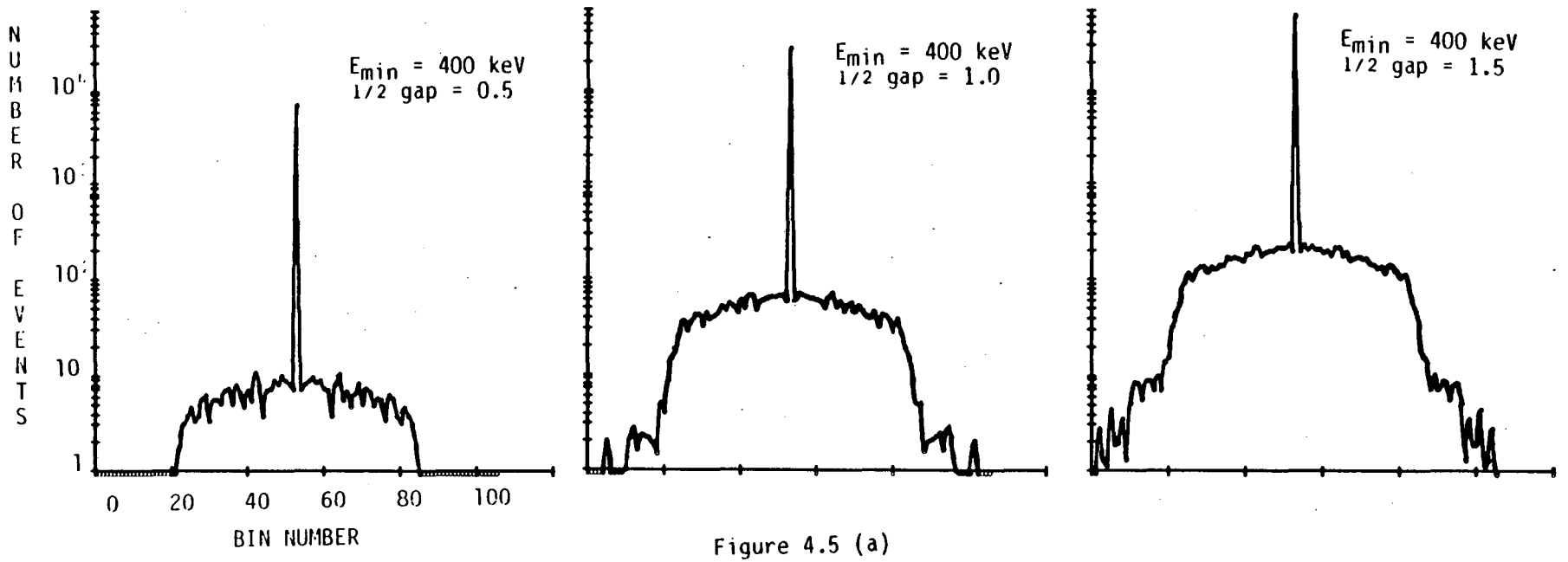

Figure 4.5 (a)

Logarithmic plot of scatter background in projection as a function of effective slice thickness. The attenuator consists of a central line parallel to the axis of a uniform, water-filled cylindrical attenuator with a diameter of 20 cm, and the energy cutoff is 400 KeV. The bin width is 0.552 cm.

SCATTER HISTOGRAM

IMAGE PLANE CENTERED AT Z= 0. CM. WITH THICKNESS= 1.00 CM. EMIN=400.00 KEV.

	0	1	2	3	4	5	6	% OR MORE	SCATTERED AT LARGE ANGLES
0	9424.62	171.22	17.54	1.82	0.	0.	0.	0.	
1	169.48	48.58	6.09	.58	0.	0.	0.	0.	
2	11.58	5.22	0.	0.	0.	0.	0.	0.	
3	.46	0.	0.	0.	0.	0.	0.	0.	
4	0.	0.	0.	0.	0.	0.	0.	0.	
5	0.	0.	0.	0.	0.	0.	0.	0.	
6	0.	0.	0.	0.	0.	0.	0.	0.	
% OR MORE	0.	0.	0.	0.	0.	0.	0.	0.	

SCATTERS BY SECOND PERSON

SCATTER HISTOGRAM

IMAGE PLANE CENTERED AT Z= 0. CM. WITH THICKNESS= 2.00 CM. EMIN=400.00 KEV.

	0	1	2	3	4	5	6	% OR MORE	SCATTERED AT LARGE ANGLES
0	29656.74	1392.72	120.95	7.61	.48	0.	0.	0.	
1	1341.75	269.56	42.52	3.65	0.	0.	0.	0.	
2	114.56	36.57	1.51	0.	0.	0.	0.	0.	
3	3.56	.56	.45	0.	0.	0.	0.	0.	
4	0.	0.	0.	0.	0.	0.	0.	0.	
5	0.	0.	0.	0.	0.	0.	0.	0.	
6	0.	0.	0.	0.	0.	0.	0.	0.	
% OR MORE	0.	0.	0.	0.	0.	0.	0.	0.	

SCATTERS BY SECOND PERSON

SCATTER HISTOGRAM

IMAGE PLANE CENTERED AT Z= 0. CM. WITH THICKNESS= 3.00 CM. EMIN=400.00 KEV.

	0	1	2	3	4	5	6	% OR MORE	SCATTERED AT LARGE ANGLES
0	67242.84	4566.55	395.60	16.54	1.48	0.	0.	0.	
1	4471.56	1226.44	134.76	9.72	0.	0.	0.	0.	
2	468.84	127.56	9.42	.84	0.	0.	0.	0.	
3	15.20	3.01	1.67	0.	0.	0.	0.	0.	
4	.78	0.	0.	0.	0.	0.	0.	0.	
5	0.	.33	0.	0.	0.	0.	0.	0.	
6	0.	0.	0.	0.	0.	0.	0.	0.	
% OR MORE	0.	0.	0.	0.	0.	0.	0.	0.	

SCATTERS BY SECOND PERSON

Figure 4.5 (b)

LINSRC scatter histograms for the simulations in Figure 4.5(a).

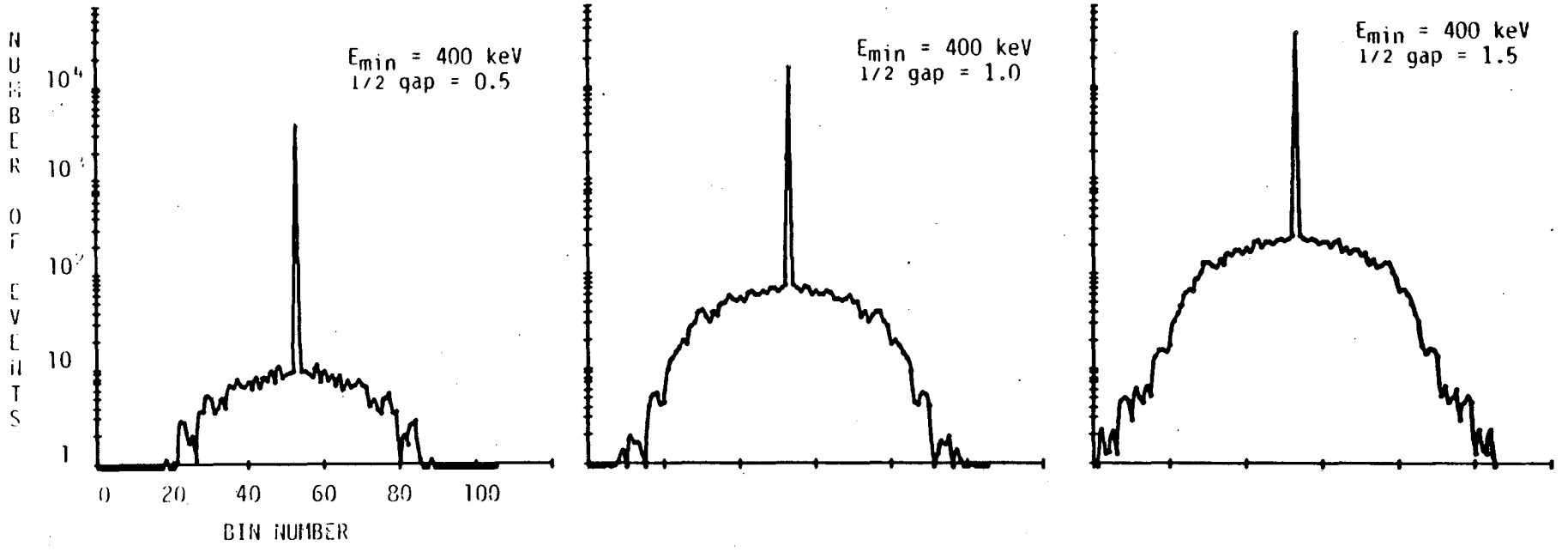

Figure 4.6 (a)

Logarithmic plot of scatter background in projection as a function of effective slice thickness. The attenuator consists of a central line parallel to the axis of a uniform, water-filled cylindrical attenuator with a diameter of 30 cm, and the energy cutoff is 400 KeV. The bin width is 0.552 cm.

SCATTER HISTOGRAM

IMAGE PLANE CENTERED AT Z= 0. CM. WITH THICKNESS= 1.00 CM. EMIN=400.00 KEV.

	0	1	2	3	4	5	6	% OF PCBE	SCATTERS AT EARTH SURFACE
0	42861.75	154.77	21.13	1.15	0.	0.	0.	0.	
1	134.65	66.26	5.33	1.42	0.	0.	0.	0.	
2	24.54	6.66	.06	0.	0.	0.	0.	0.	
3	2.51	0.	0.	0.	0.	0.	0.	0.	
4	0.	0.	0.	0.	0.	0.	0.	0.	
5	0.	0.	0.	0.	0.	0.	0.	0.	
6	0.	0.	0.	0.	0.	0.	0.	0.	
% OF PCBE	0.	0.	0.	0.	0.	0.	0.	0.	

SCATTERS AT
SECOND EMISSION

SCATTER HISTOGRAM

IMAGE PLANE CENTERED AT Z= 0. CM. WITH THICKNESS= 2.00 CM. EMIN=400.00 KEV.

	0	1	2	3	4	5	6	% OF PCBE	SCATTERS AT EARTH SURFACE
0	17176.46	1225.76	159.10	14.55	0.	0.	0.	0.	
1	1117.50	512.88	66.25	7.22	.35	0.	0.	0.	
2	165.01	67.16	9.50	0.	0.	0.	0.	0.	
3	15.51	3.26	.45	0.	0.	0.	0.	0.	
4	0.	0.	0.	0.	0.	0.	0.	0.	
5	0.	0.	0.	0.	0.	0.	0.	0.	
6	0.	0.	0.	0.	0.	0.	0.	0.	
% OF PCBE	0.	0.	0.	0.	0.	0.	0.	0.	

SCATTERS AT
SECOND EMISSION

SCATTER HISTOGRAM

IMAGE PLANE CENTERED AT Z= 0. CM. WITH THICKNESS= 2.00 CM. EMIN=400.00 KEV.

	0	1	2	3	4	5	6	% OF PCBE	SCATTERS AT EARTH SURFACE
0	38744.62	4054.62	514.17	42.22	.44	0.	0.	0.	
1	3613.25	1664.69	244.42	21.66	1.25	0.	0.	0.	
2	537.65	221.09	36.67	0.	0.	0.	0.	0.	
3	49.29	17.22	1.69	0.	0.	0.	0.	0.	
4	1.74	0.	.52	0.	0.	0.	0.	0.	
5	0.	0.	0.	0.	0.	0.	0.	0.	
6	0.	0.	0.	0.	0.	0.	0.	0.	
% OF PCBE	0.	0.	0.	0.	0.	0.	0.	0.	

SCATTERS AT
SECOND EMISSION

Figure 4.6 (b)

LINSRC scatter histograms for the simulations in Figure 4.6(a).

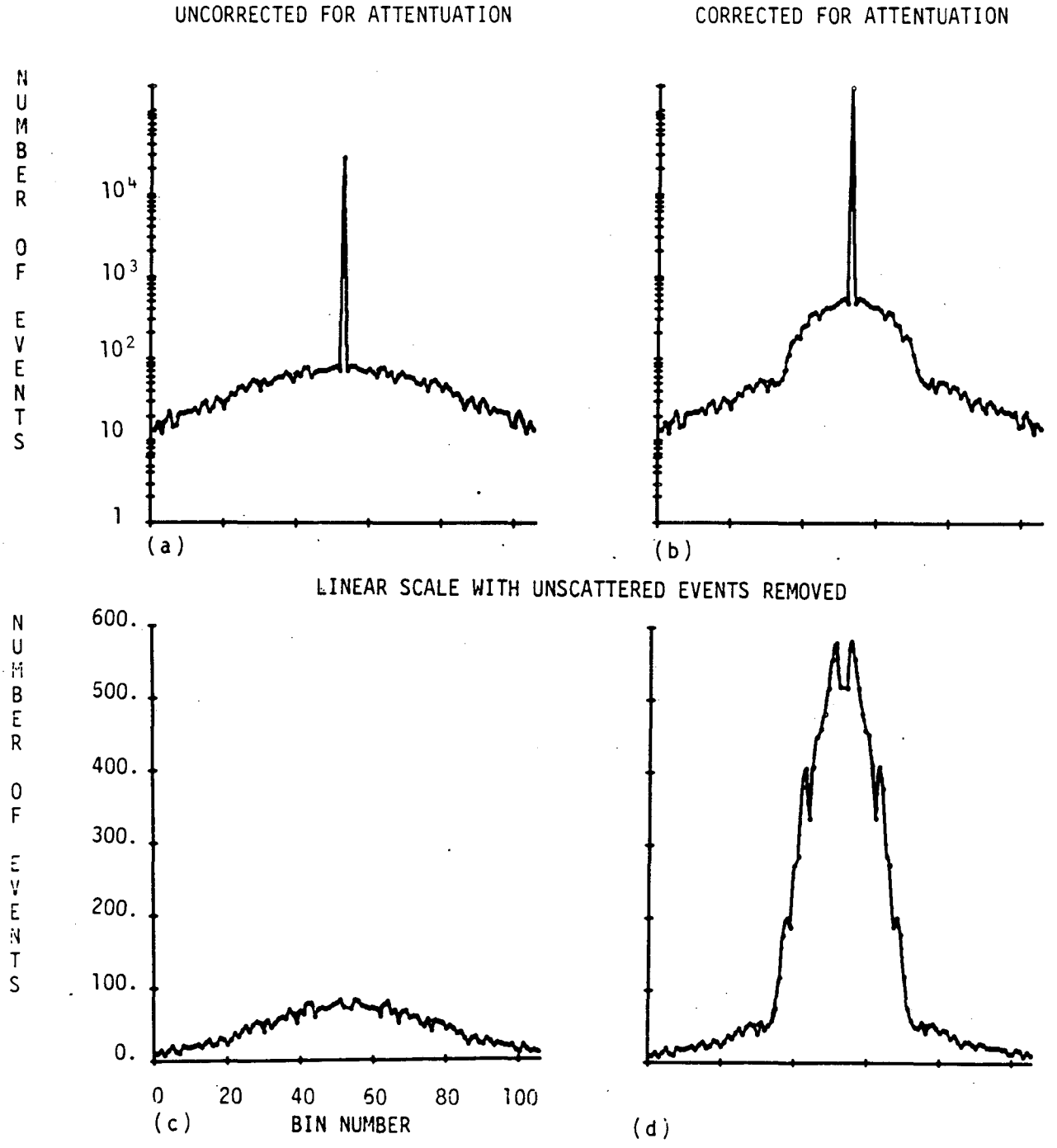

Figure 4.7

The effect of attenuation-correction on scatter background in projection. The source is a central line in a 20 cm uniform attenuating cylinder. The energy cutoff is 300 keV, and the effective slice thickness is 1.0 cm. (a) uncorrected, logarithmic scale; (b) corrected, logarithmic scale; (c) uncorrected, linear scale; (d) corrected, linear scale. The bin size is 0.552 cm.

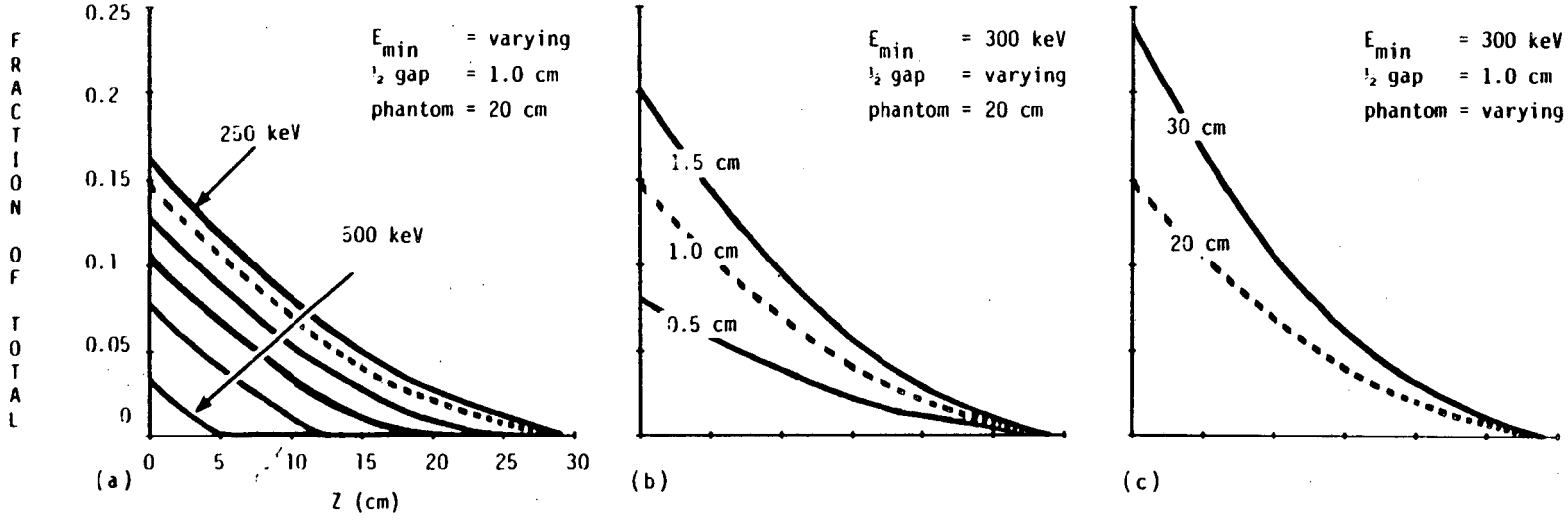

Figure 4.8

Fraction of total events which a detection system erroneously places on chords which lie a distance Z or greater from the actual source position. A point on any of the curves above is obtained by integrating the corresponding composite projection from z = Z to the edge of the projection, and then dividing the result by the total number of events. The abscissa is the lower limit of integration, Z. The source is a line at the center of a cylinder filled with water, parallel to the axis of the cylinder. Its projection position is z = 0. (a) as a function of energy cutoff: 250,300,350,400,450 and 500 KeV for a half-gap of 1 cm and a 20 cm attenuator; (b) as a function of effective slice thickness for an energy cutoff of 300 KeV and a 20 cm attenuator; (c) as a function of attenuator diameter for an energy cutoff of 300 KeV and a 1.0 cm half-gap.

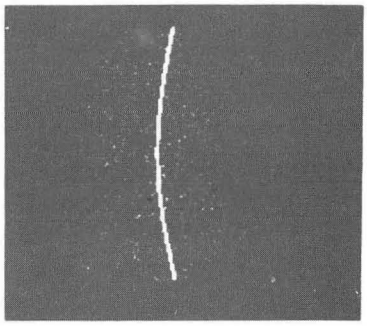

E_{min} = 250 keV
1/2 gap = 0.5

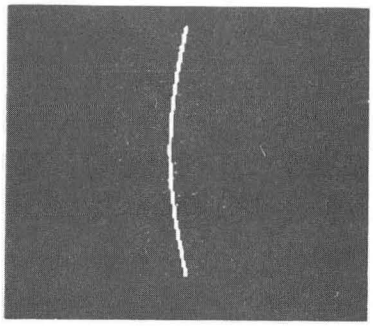

E_{min} = 350 keV
1/2 gap = 0.5

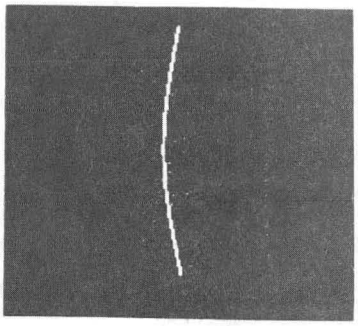

E_{min} = 450 keV
1/2 gap = 0.5

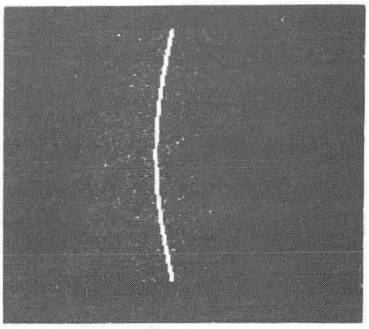

E_{min} = 250 keV
1/2 gap = 1.0

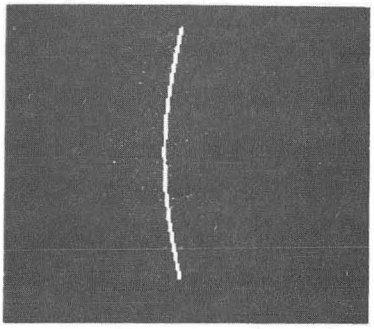

E_{min} = 350 keV
1/2 gap = 1.0

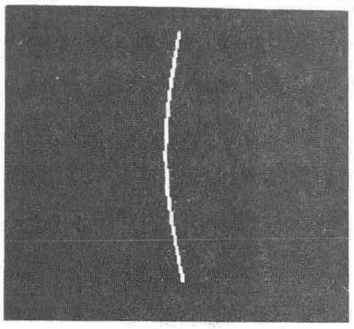

E_{min} = 450 keV
1/2 gap = 1.0

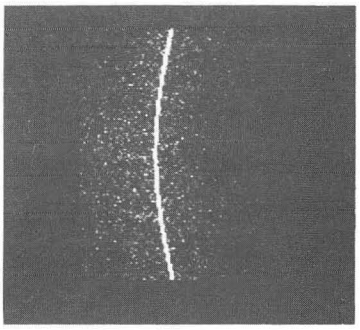

E_{min} = 250 keV
1/2 gap = 1.5

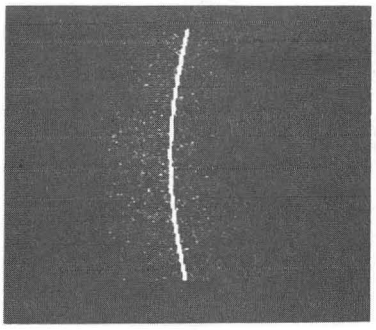

E_{min} = 350 keV
1/2 gap = 1.5

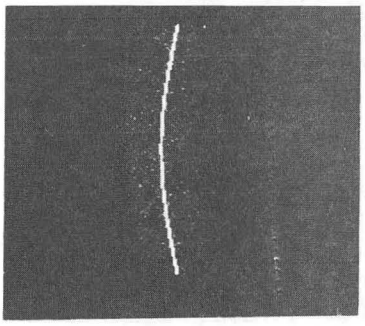

E_{min} = 450 keV
1/2 gap = 1.5

Figure 4.9

XBB 830-10816

Sinogram display for a simulated detection system showing scatter background as a function of energy cutoff and effective slice thickness. The width of each sinogram (ordinate) is 64 cm and the angular range (abscissa) is from 0^{o} at lower left to 180^{o} at upper left. The grey scale is **linear** and **no attenuation correction** has been performed. The source is a line parallel to the axis of a 20 cm uniform attenuating cylinder and the coordinates of the source are x=5, y=0.

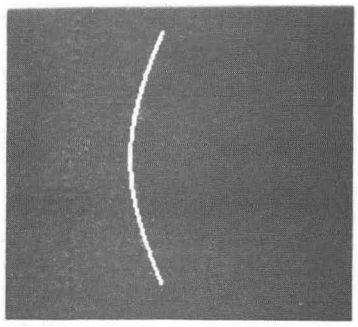

E_{min} = 250 keV
1/2 gap = 0.5

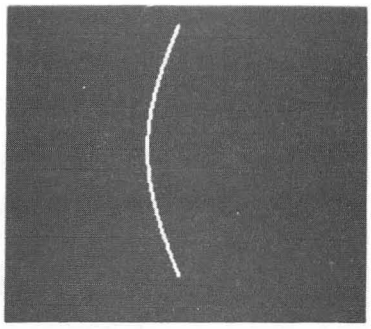

E_{min} = 350 keV
1/2 gap = 0.5

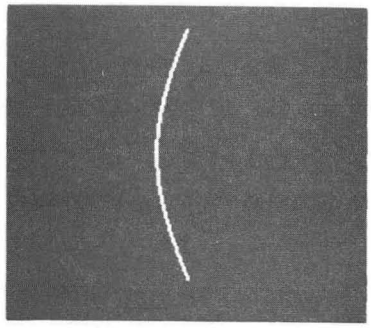

E_{min} = 450 keV
1/2 gap = 0.5

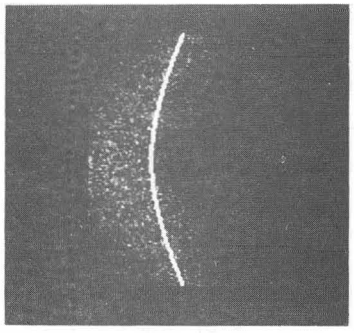

E_{min} = 250 keV
1/2 gap = 1.0

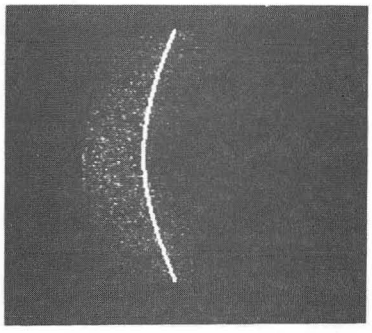

E_{min} = 350 keV
1/2 gap = 1.0

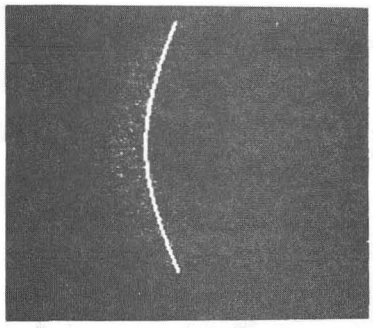

E_{min} = 450 keV
1/2 gap = 1.0

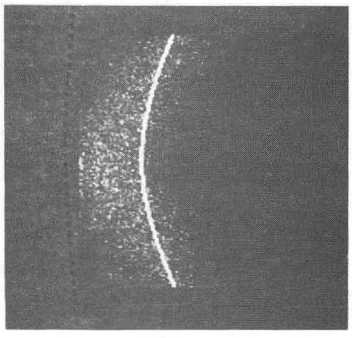

E_{min} = 250 keV
1/2 gap = 1.5

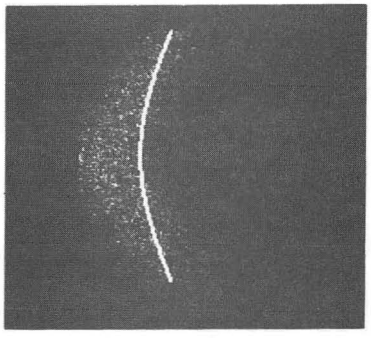

E_{min} = 350 keV
1/2 gap = 1.5

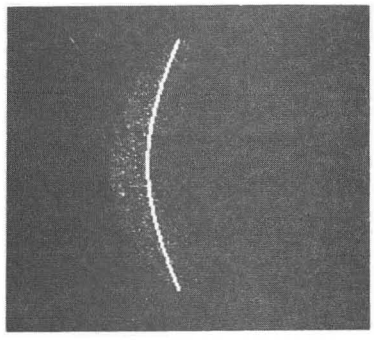

E_{min} = 450 keV
1/2 gap = 1.5

Figure 4.10

XBB 830-10815

Sinogram display for a simulated detection system showing scatter background as a function of energy cutoff and effective slice thickness. The width of each sinogram (ordinate) is 64 cm and the angular range (abscissa) is from 0^{o} at lower left to 180^{o} at upper left. The grey scale is **linear** and **no attenuation correction** has been performed. The source is a line parallel to the axis of a 20 cm uniform attenuating cylinder and the coordinates of the source are x=9.5, y=0.

References

1. Derenzo SE: Method for optimizing side shielding in positron emission tomographs and for comparing detector materials. J Nucl Med 21: 971-977, 1980

2. Dresser MM and Knoll GF: Results of scattering in radioisotope imaging. IEEE Trans Nucl Sci NS-20: No 1, 266-272, 1973

3. Phelps ME, Hoffman EJ, Huang SC and Kuhl DE: ECAT: A new computerized tomographic imaging system for positron-emitting radiopharmaceuticals. J Nucl Med 19: 635-647, 1978

4. Pang SC and Genna S: The effect of Compton scattered photons on emission computerized transaxial tomography. IEEE Trans Nucl Sci NS-26: No 2, 2772-2774, 1979

5. Brooks RA, Sank VJ, Friauf WS, Leighton SB, Cascio HE and DiChiro G: Design considerations for positron emission tomography. IEEE Trans Biomed Eng BME-28: No 2, 158-177, 1981

6. Hoffman EJ, Phelps ME, Huang SC, Plummer D, and Kuhl DE: Evaluating the performance of multiplane positron tomographs designed for brain imaging. IEEE Trans Nucl Sci NS-29: No 1, 469-473, 1982

7. Ueda K, Tanaka E, Takami K, Kawaguchi F, Okajima K and Ishimatsu K: Evaluation of slice shield collimators for multi-layer positron emission computed tomographs. IEEE Trans Nucl Sci NS-29: No 1, 563-566, 1982

8. Yamamoto M, Ficke DC, and Ter-Pogossian MM: Performance study of PETT VI, a positron computed tomograph with 288 cesium fluoride detectors. IEEE Trans Nucl Sci NS-29: No 1, 529-533, 1982

9. Beck JW, Jaszczak RJ, and Starmer CF: Analysis of SPECT using Monte Carlo simulation. Proceedings of the International Workshop on Physics and Engineering in Medical Imaging, IEEE Cat No 82CH1751-7, pp 32-38, 1982

10. Beck JW, Jaszczak RJ, Coleman RE, Starmer CF and Nolte LW: Analysis of SPECT including scatter and attenuation using sophisticated Monte Carlo modeling methods. IEEE Trans Nucl Sci NS-29: No 1, 506-511, 1982

11. Logan J and Bernstein HJ: A Monte Carlo simulation of Compton scattering in positron emission tomography. J Comput Assist Tomogr 7: 316-320, 1983

12. Evans RD: The Atomic Nucleus. New York, McGraw-Hill, 1955, pp 600-719

13. Budinger TF, Derenzo SE, Gullberg GT, Greenberg WL, and Huesman RH: Emission computer assisted tomography with single-photon and positron annihilation photon emitter. J Comput Assist Tomogr 1: 131-145, 1977

14. Derenzo SE, Budinger TF, Huesman, RH, Cahoon JL and Vuletich T: Imaging properties of a positron tomograph with 280 BGO crystals. IEEE Trans Nucl Sci NS-28: No 1, 81-89, 1981

This report was done with support from the Department of Energy. Any conclusions or opinions expressed in this report represent solely those of the author(s) and not necessarily those of The Regents of the University of California, the Lawrence Berkeley Laboratory or the Department of Energy.

Reference to a company or product name does not imply approval or recommendation of the product by the University of California or the U.S. Department of Energy to the exclusion of others that may be suitable.

TECHNICAL INFORMATION DEPARTMENT
LAWRENCE BERKELEY LABORATORY
UNIVERSITY OF CALIFORNIA
BERKELEY, CALIFORNIA 94720